1 **W-band S/Z Relationships for Rimed Snow Particles: Observational Evidence from**

2 **Combined Airborne and Ground-based Observations**

4 Shelby Fuller [1], Sam Marlow [1], Samuel Haimov [1], Matthew Burkhart [1], Kevin Shaffer [1], Austin

5 Morgan [1], and Jefferson R. Snider [1,2]

7 [1] Department of Atmospheric Science, University of Wyoming, Laramie, WY, USA
8
9
10
11 [2] Corresponding Author, jsnider@uwyo.edu

13    **Abstract**

14    Values of undercatch-corrected liquid-equivalent snowfall rate (S) at a ground site and

15    microwave reflectivity (Z) retrieved using an airborne W-band radar were acquired during

16    overflights. The temperature at the ground site was between -6 and -15 $^{o}$C. At flight level, within

17    clouds containing ice and supercooled liquid water, the temperature was approximately 7 $^{o}$C

18    colder. Additionally, airborne measurements of snow particle imagery were acquired. The

19    images demonstrate that most of the snow particles were rimed, at least a flight level. A

20    relatively small set of S/Z pairs (4) are available from the overflights. Important distinctions

21    between these measurements and those of Pokharel and Vali (2011), who reported S/Z pairs and

22    an S/Z relationship for rimed snow particles, are 1) the fewer number of S/Z pairs, 2) the method

23    used to acquire S, and 3) the altitude, relative to ground, of the W-band Z retrievals. This

24    analysis corroborates that the S/Z relationship reported in Pokharel and Vali (2011) yields an S -

25    in scenarios with snowfall produced by riming - substantially larger than that derived using an

26    S/Z relationship developed for unrimed snow particles.

## 1 - Introduction

Improvement of methods used to measure snowfall and rainfall are an ongoing focus of meteorological research. The various methods are ground-based instruments that evaluate the mass of precipitation that falls into or onto a collector (precipitation gauges) (Brock and Richardson 2001), ground-based radars (Wilson and Brandes 1979), and airborne and space-borne radars (Matrosov 2007; Kulie and Bennartz 2009; Geerts et al. 2010; Skofronick-Jackson et al. 2017). An objective of these approaches, whether used to make observations independent of other methods (e.g., Kulie and Bennartz 2009), or as a component of multiple observations (e.g., Cocks et al. 2016), is estimation of precipitation rate and accumulated precipitation amount

Many studies have investigated using radar for evaluating rainfall (for a review see Wilson and Brandes 1979). There are two approaches. The first is research, both observational and computational, that probes the relationship between rainfall rate (R) and radar-measured values of range-corrected backscattered microwave power. The latter is commonly reported as an equivalent radar reflectivity factor ($Z_e$). The second is operational in the sense that precipitation gauges are used to calibrate measurements acquired using weather surveillance radars. Complications associated with converting $Z_e$ to R, or converting a radar reflectivity factor[1] (Z) to R, can be grouped in four categories: 1) Inaccuracy in quantification of Z, 2) variation of the R/Z relationship stemming from precipitation processes (e.g., coalescence and break up), 3) difference between the volume of a radar range gate versus the much smaller volume of atmosphere sampled as precipitation falls to a gauge, and 4) vertical displacement between a radar range gate and a calibrating gauge, especially at far ranges.

---

[1] Radars are calibrated to report $Z_e$ (Smith 1984). Herein, radar reflectivities are reported as $Z = Z_e$ and as dBZ = $10\log_{10}(Z_e)$.

50    For situations with snowfall, methods employing either gauge or radar are associated

51    with complications beyond that incurred in rainfall (Matrosov 2007; Martinaitis et al. 2015;

52    Cocks et al. 2016). Problems associated with gauge measurements are wind-induced snow

53    particle undercatch, gauge capping, delayed registration, and blowing snow aliasing as snowfall.

54    Moreover, in a situation with snow particles more abundant within a radar range gate, compared

55    to rain drops, and where a measurement of Z is used to infer R via a R/Z relationship, the

56    resultant precipitation rate will likely be inaccurate. This is because hydrometeor shape, density,

57    and dielectric properties are all variable for snow particles while relatively invariant for rain

58    drops. Additionally, a snow particle's terminal fall speed varies with size (as is the case for

59    drops) and with particle shape and particle density. Going forward, we refer to the latter two

60    properties as shape and density.

61    The goals of this paper are as follows: 1) to describe measurements of undercatch-

62    corrected liquid-equivalent snowfall rate (S, mm h$^{-1}$) and how these were paired with W-band

63    measurements of reflectivity (Z, mm$^6$ m$^{-3}$) ; 2) to contrast the S/Z pairs against S/Z relationships

64    commonly applied in radar retrievals of S; and 3) to investigate why the S/Z pairs deviate from

65    predictions of some S/Z relationships.

66    In calculations of paired values of S and Z, density is an important parameter. Density is

67    commonly estimated using empirical data (e.g., Pokharel and Vali 2011, [PV11]). For graupel, a

68    snow particle that grows via collection of supercooled cloud droplets in a process commonly

69    referred to as riming, paired observations of particle mass and particle size have been used to

70    estimate density. There is considerable uncertainty in this approach. Based on data collected at

71    two northwestern US surface sites (Zikmunda and Vali 1972; Locatelli and Hobbs 1974), density

72    values differ by at least a factor of two at particle sizes smaller than 2000 μm (PV11; their Fig.

73   4). Given that the density of rime ice varies with droplet impact speed, droplet size, and

74   temperature (Macklin 1962), it is not surprising that the density-size relationships analyzed by

75   PV11 are so varied.

76       Table 1 and the following paragraphs overview W-band S/Z relationships applied in

77   instances with snow particles grown by vapor deposition (crystal), by collection of crystals

78   (aggregate snowflake), and by riming (rimed crystal and graupel). Henceforth, the latter two

79   snow particle types are collectively referred to as rimed snow particles.

80       In a computational study, Hiley et al. (2011) considered a variety of snow particle types

81   (column, plate, bullet rosette, sector plate, dendrite, and aggregate snowflake), employed a

82   parameterized ice particle size distribution (PSD) function (Field et al. 2005), accounted for a

83   range of temperature (-5 to -15 $^{\circ}$C) via the Field et al. parameterization, and developed a range of

84   S/Z relationships for snow particles. Except for the aggregate snowflakes (henceforth,

85   aggregates), the modeled particle types were vapor-grown crystals. Hiley et al.'s upper- and

86   lower-limit relationships are $S = 0.21 \cdot Z^{0.77}$ and $S = 0.024 \cdot Z^{0.91}$, respectively. Matrosov (2007)

87   developed an S/Z relationship for aggregates. In that work, parameterized PSDs from Braham

88   (1990) were employed, and a range of particle aspect ratios were factored into the calculations.

89   For aggregates, the S/Z relationship is $S = 0.056 \cdot Z^{1.2}$ (Matrosov 2007). It should be noted that

90   Hiley et al. (2011) and Matrosov (2007) employed similar, but not identical, computational

91   methods. Computational research was also conducted by Kulie and Bennartz (2009) who

92   adopted the wavelength-dependent density derived by Surussavadee and Staelin (2007) (200 kg

93   m$^{-3}$ at $\lambda = 3.2$ mm), modeled the snow particles as spheres, and applied PSDs based on Field et

94   al. The resultant S/Z is $S = 0.52 \cdot Z^{0.83}$ (Surussavadee and Staelin 2007; Kulie and Bennartz 2009;

95   henceforth, SSKB). Variance in the calculations discussed in this paragraph originate from

96    changes in density, shape, fall speed, PSD, and particle size as these changes are propagated

97    through the cloud-microphysical and microwave-scattering calculations.

98         In a hybrid approach (computational and an analysis of measurements), PV11 concluded

99    that most of the snow particles they imaged were rimed snow particles. Values of S were

100    calculated using a density-size function ($\rho_1$, discussed below), a fall speed-size function,

101    measured PSDs and measured particle images, and a determination of particle volumes. It was

102    assumed that a prolate spheroid approximated particle shape and that shape  was the basis for

103    determining a particle's sphere-equivalent volume and the particle's sphere-equivalent size. The

104    sphere-equivalent size was applied in the two functions. Values of Z were calculated using a

105    measured PSD, sphere-equivalent sizes, the $\rho_1$ function, and Mie Theory. PV11 presented

106    calculations of Z, obtained using two density-size relationships (their Eqs. 1 and 2) and compared

107    their calculated reflectivities to measurements of Z from a W-band radar. That led to their

108    conclusion that "...the lower density assumption…yielded closer correspondence to observed

109    reflectivities." Their recommendation for S as a function of measured Z - hereafter the $S(\rho_1)/Z$

110    best-fit line - is $S = 0.39 \cdot Z^{0.58}$. Values of Z that were paired with the calculated values of S (i.e.,

111    the S/Z pairs from PV11 that we present in Sect. 4), and that were used to determine the $S(\rho_1)/Z$

112    best-fit line, came from the W-band radar. In addition to variance in their values of S, coming

113    from a dependence on density, PV11 state that a value of S derived via their best-fit line is

114    uncertain by a factor-of-ten. That uncertainty is evident in the variance of S/Z data pairs about

115    the $S(\rho_1)/Z$ line in Fig. 11 of PV11. Those investigators, and Geerts et al. (2010), attributed the

116    variance to use of two-dimensional snow particle images in calculations of S and to actual

117    variations of density, shape, and particle size not accounted for in the calculations.

118    Another set of hybrid-type S/Z relationships was developed by Falconi et al. (2018; their

119    Table 2). These are based on measurements from a video disdrometer, weighing precipitation

120    gauge, microwave radiometer, and a vertically-pointing W-band radar. All these systems were

121    operated at the ground. The data set was stratified into intervals of lightly-rimed, moderately-

122    rimed, and heavily-rimed snow. A proxy for snow particle riming - radiometer measurements of

123    liquid water path – was the basis for the stratifications (von Lerber et al. 2017). The S/Z

124    relationships are $S = 0.10 \cdot Z^{1.0}$ (lightly-rimed), $S = 0.079 \cdot Z^{1.3}$ (moderately-rimed), and $S =$

125    $0.060 \cdot Z^{1.4}$ (heavily-rimed).

126    Our focus is on surface measurements of S and on pairing of those measurements with

127    airborne measurements of Z. We also analyze airborne measurements of snow particle imagery.

128    The latter demonstrate that the particles observed at flight level were rimed. The imagery is the

129    basis for our assertion that our data set is relevant to ongoing investigations of using Z to

130    evaluate S in situations where precipitation is produced by riming.

131    Section 2 describes the setting of our study, the instruments we deployed, and recordings

132    we obtained using two data acquisition systems. One of the data systems was operated at a

133    ground site and the other on an aircraft. Section 3 is an analysis of the recordings; this section

134    also considers recordings from two additional, but ancillary, ground sites. Our findings are

135    discussed in Sect. 4 and summarized in Sect. 5. An Appendix (Sect. 6) explains how we

136    averaged recordings of near-surface W-band reflectivities and surface-based recordings of

137    snowfall.

138    Table 1 – W-band S/Z relationships from the literature, snow particle type, and values of minimum relative S difference

| Reference | Abbreviation used for reference | S/Z relationship | Snow Particle Type | Minimum relative S deference on December 15 2016 [a] | Minimum relative S difference on January 3 2017 [a] |
|---|---|---|---|---|---|
| Hiley et al. (2011) | - | $S=0.21 \cdot Z^{0.77}$ | Upper-limit S/Z relationship for vapor-grown crystals | 0.7 | 1.0 |
| Matrosov (2007) | - | $S=0.056 \cdot Z^{1.2}$ | Aggregates | 1.4 | 8.5 [b] |
| Surussavadee and Staelin (2007) and Kulie and Bennartz (2009) | SSKB | $S=0.52 \cdot Z^{0.83}$ | Spherical snow particles with density = 200 kg m$^{-3}$ | 0.3 | 0.2 [c] |
| Pokharel and Vali (2011) | PV11 | $S=0.39 \cdot Z^{0.58}$ | Rimed snow particles assuming the lower of two density-size relationships | 0.3 | 0.0 [d] |
| Falconi et al. (2018) | - | $S=0.060 \cdot Z^{1.4}$ | Snow particles classified as heavily rimed | 0.6 [e] | 8.5 |

139

140    [a] Minimum relative S difference is defined as the minimum of $|(S_{HP}-S)|/S$ where $S_{HP}$ is a measurement of undercatch-corrected liquid-equivalent
141    snowfall rate (Table 6) and S is a snowfall rate on an S/Z relationship line evaluated at one of the attenuation-corrected reflectivities (Sect. 4).

142    [b] Attenuation-corrected Z on this day (0.6 mm$^6$ m$^{-3}$) is smaller than the lower-limit Z (1 mm$^6$ m$^{-3}$) advised for this S/Z relationship (Matrosov
143    2007).

144    [c] Maximum relative S difference on this day is 0.4.

145    [d] Maximum relative S difference on this day is 0.7.

146    [e] Maximum relative S difference on this day is 0.9.

147

## 2 - Site, Aircraft, and Instruments

148

### 2.1 - Site

149

150     Analyzed herein are aircraft and ground data from 14/15 December 2016 and from 3

151 January 2017. The ground data were acquired in a forest/prairie ecotone on the eastern slope of

152 the Medicine Bow Mountains in southeast Wyoming (Figs. 1a-b). No ground-based observers

153 were deployed during the two snowfall events analyzed.

154     At one of three ground sites (HP in Figs. 1a-b) a hotplate precipitation gauge (Rasmussen

155 et al. 2011; Zelasko et al. 2018), a GPS receiver, and a data acquisition system were deployed.

156 Once per second, the data system ingested a hotplate-generated data string, combined that with

157 time-of-day from the GPS receiver [Coordinated Universal Time (UTC)], and recorded the

158 merged hotplate/UTC data string. The absolute accuracy of the time stamp is no worse than 2 s.

159     Overflights of the hotplate were done by the University of Wyoming King Air (WKA) on

160 14/15 December 2016 and on 3 January 2017. The flights were conducted in preparation for the

161 SNOWIE field project (Tessendorf et al. 2019) and were flown from the Laramie, WY Airport

162 (LA in Fig. 1a). Data acquisition on the WKA was also synchronized with UTC, but with much

163 better accuracy than at the hotplate.

164

165   Measurements of horizontal wind (speed and direction), temperature, relative humidity,

166 and pressure from the US-GLE AmeriFlux tower (AF in Figs. 1a-b) are also components the

167 analysis. The AmeriFlux data were provided to us as 30-minute averages (AmeriFlux 2021;

168 Marlow et al. 2023).

169
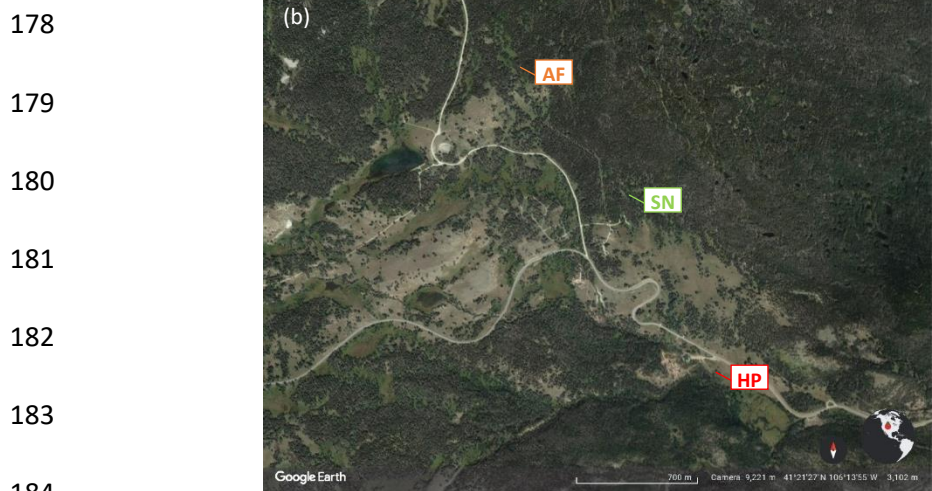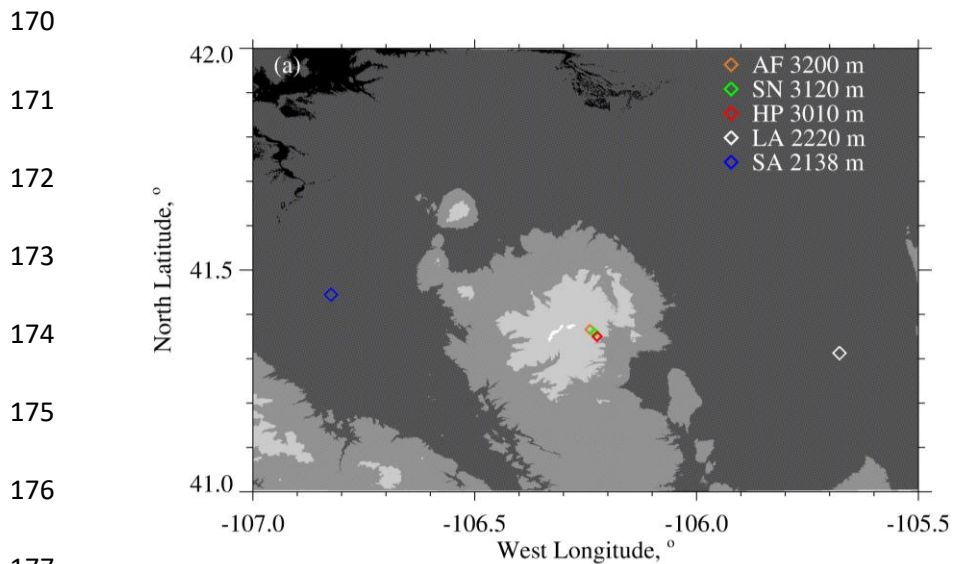
Figure 1 – (a) Southeast Wyoming, airport at Saratoga, WY (SA), airport at Laramie, WY (LA),

and the ground sites: AF = US-GLE AmeriFlux tower, SN = Brooklyn Lake SNOTEL, and HP =

hotplate. Altitudes of the airports and ground sites are in the legend. Altitude thresholds for the

digital elevation map are 1500, 2000, 2500, 3000, and 3500 meters. (b) Close up of the AF, SN,

and HP ground sites (from © Google Earth).

192 **2.2 - University of Wyoming King Air (WKA)**

193    The following WKA measurements were analyzed: aircraft position, temperature, snow

194 particle imagery, and three moments of the cloud droplet size distribution function. A Cloud

195 Droplet Probe (CDP; Faber et al. 2018) was the basis for the droplet size distribution

196 measurements and the derived moments. The latter are droplet concentration (N), cloud liquid

197 water content (LWC), and mean droplet diameter (<D>). Snow particle imagery was obtained

198 using a precipitation particle imaging probe (2DP; Korolev et al. 2011) and a cloud particle

199 imaging probe (2DS; Lawson et al. 2006). These acquired two-dimensional images of particles

200 between 200 to 6400 μm (2DP) and between 10 to 1280 μm (2DS).

201 **2.3 – The W-band Wyoming Cloud Radar (WCR)**

202    Retrievals from the up-looking and down-looking antennas of the WCR, operated on the

203 WKA, were also analyzed. For this we used Level 2 WCR data[2] with reflectivities recorded as

204 $dBZ = 10 \cdot \log_{10}(Z)$. The reflectivities were converted from dBZ to Z prior to processing.

205 Additionally, values of the vertical-component Doppler velocity retrieved from below the WKA

206 using the WCR's down-looking antenna were analyzed. The Doppler velocities were corrected

207 for aircraft motion as described in Haimov and Rodi (2013). We use $V_D$ to symbolize the

208 corrected vertical-component Doppler velocity and adopt the convention that $V_D > 0$ indicates

209 upward hydrometeor motion.

210

---

[2] http://flights.uwyo.edu/uwka/wcr/projects/snowie17/PROCESSED_DATA/

211     The Level 2 WCR sampling was different on the two flight days and this difference is

212 shown in Table 2. Ground-based calibrations of the WCR's up-looking antenna and correlations

213 between in-flight retrievals acquired using the WCR's up-looking and down-looking antennas

214 were used to estimate the precision and absolute accuracy of the WCR-derived values of dBZ.

215 These are $\pm$ 1.0 dBZ and $\pm$ 2.5 dBZ, respectively (PV11).

216

217    Table 2 – Level 2 WCR sampling and the WKA overflight time

218

| Date | Level 2 WCR Vertical Sampling, m | Level 2 WCR Along-track Sampling, s | Overflight Time, UTC |
|---|---|---|---|
| 14/15 December 2016 | 23 | 0.23 | 00:00:38 (15 December 2016) |
| 3 January 2017 | 30 | 0.36 | 20:32:03 |

219
220

**2.4 - Hotplate Gauge**

Algorithms used to process hotplate measurements are described in Rasmussen et al. (2011), Boudala et al. (2014), and Zelasko et al. (2018). Henceforth, these are referred to as R11, B14, and Z18, respectively. This section describes how hotplate measurements acquired at the HP site were analyzed. The hotplate deployed at the HP site is described in Wolfe and Snider (2012), Z18, and in Marlow et al. (2023).

Five measurements fundamental to the steady state energy budget of the hotplate's temperature-controlled up-viewing plate are output by the hotplate microprocessor as one-minute running averages (Z18). These averages were merged with the GPS time and recorded at 1 Hz by the data acquisition system (Sect. 2.1). With these measurements, calibration data (Marlow et al. 2023), and the algorithm developed by Z18, we calculated S in two steps. First, the five hotplate measurements (electrical power supplied to the plate, ambient temperature, wind speed, downwelling shortwave flux, and downwelling longwave flux) were input to Eq. 3 in Z18. The output of that equation is a provisional liquid-equivalent precipitation rate. Second, the snow particle catch efficiency, described in the next paragraph, was used to calculate S as the ratio of the provisional rate and the catch efficiency.

Marlow et al. (2023; their Fig. 3b) report the relationship between snow particle catch efficiency and wind speed that was applied in the calculation of S. There are three bases for this relationship. First is the catch efficiencies R11 derived using measurements obtained from a weighing gauge, operated within a double fence intercomparison reference shield, and collocated measurements from an unshielded hotplate gauge. These paired measurements are symbolized SRG (shielded reference gauge) and UHG (unshielded hotplate gauge). R11 plotted hotplate catch efficiencies (i.e., UHG/SRG) versus wind speeds measured at 10 m AGL (their Fig. 8).

244 Second is Marlow et al.'s adjustment of R11's 10 m AGL wind speeds to 2 m AGL. The basis

245 for the adjustment is surface boundary layer parameters derived for R11's site (Kochendorfer et

246 al. 2018) and an equation from Panofsky and Dutton (1984; their Eq. 6.7). The adjustment was

247 made because the hotplate-derived wind speeds, both here and in Marlow et al. (2023), were

248 acquired at approximately 2 m above the snowpack surface. Third is Marlow et al.'s comparison

249 of SNOTEL-derived liquid-equivalent depth changes and hotplate-derived time-integrated

250 accumulations. The interval for the comparisons is 24 hours. Based on the comparison, which

251 has 57 paired values acquired at the sites labeled HP and SN in Fig. 1, the average fractional

252 absolute relative difference is 0.30. Marlow et al. also provided an estimate of the error in a

253 SNOTEL measurement (2.4 mm). At accumulation = 10 mm the error corresponds to a relative

254 error = 0.24. This indicates that SNOTEL contributed significantly to the SNOTEL/hotplate

255 variance and especially so for the smaller accumulations in Fig. 9a of Marlow et al. (2023).

256 Because of this, we do not limit the following estimate of hotplate precision to a subset of the 57

257 paired measurements. Based on our assessment of the average fractional absolute relative

258 difference, the hotplate precision applied in this analysis was taken to be 0.3.

259      The hotplate-derived wind speeds acquired at ~ 2 m, and discussed in the previous

260 paragraph, are henceforth symbolized $U_{PRO}$. The basis for these is a steady state energy budget of

261 the hotplate's temperature-controlled down-viewing plate and a proprietary algorithm (R11 and

262 Z18). The $U_{PRO}$ are reported by a hotplate as one-minute running averages (Z18) and we

263 recorded these at 1 Hz. Examples are the gray dots in Fig. 2. Additionally, we calculated and

264 analyzed one-minute-averaged values of $U_{PRO}$ and the corresponding standard deviations.

265 Examples of these are the black circles and the short vertical line segments in Fig. 2.

266

267

268

269

270

271

272
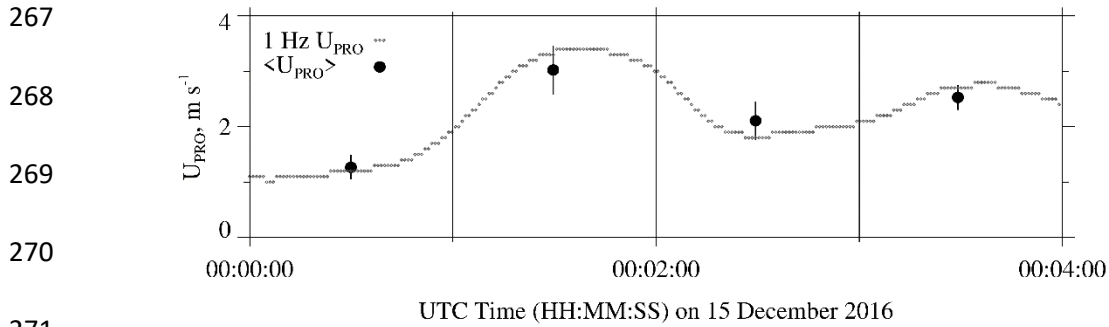
273 Figure 2 – Hotplate wind speed measurements ($U_{PRO}$) 00:00:00 to 00:04:00 on 15 December

274 2016. Gray dots are the one-minute running-average $U_{PRO}$ recorded at 1 Hz. Black circles are the

275 one-minute-averaged $U_{PRO}$ (± 1 standard deviation).

276

277    **3 - Analysis**

278    **3.1 - WKA Overflight Time**

279         The focus of our analysis is the two WKA flight segments shown in Figs. 3a-b. The maps

280    shown in the figures have the three ground sites (AF, SN, and HP) and the WKA flight tracks

281    (white line). The beginning-to-end time interval for the flight tracks is 100 s and these are

282    divided into ten 10-second intervals. The 10 s intervals are indicated with white diamonds.

283    Except for the turn evident in Fig. 3b, the flight tracks are straight, and the track direction is

284    approximately upwind to downwind.

285         Times that the WKA was closest to the HP site were evaluated by finding the point on the

286    flight track where the horizontal position of the WKA was closest to the hotplate's coordinates.

287    These times are symbolized $t_0$ and are referred to as overflight times. In Figs. 3a-b the downwind

288    end of the flight tracks end at the overflight time. The latitude/longitude position of the aircraft

289    was within 390 m of the hotplate at the overflight times. Table 2 has the overflight times on the

290    two flight days.

291

292

293

294

295

296

297

298
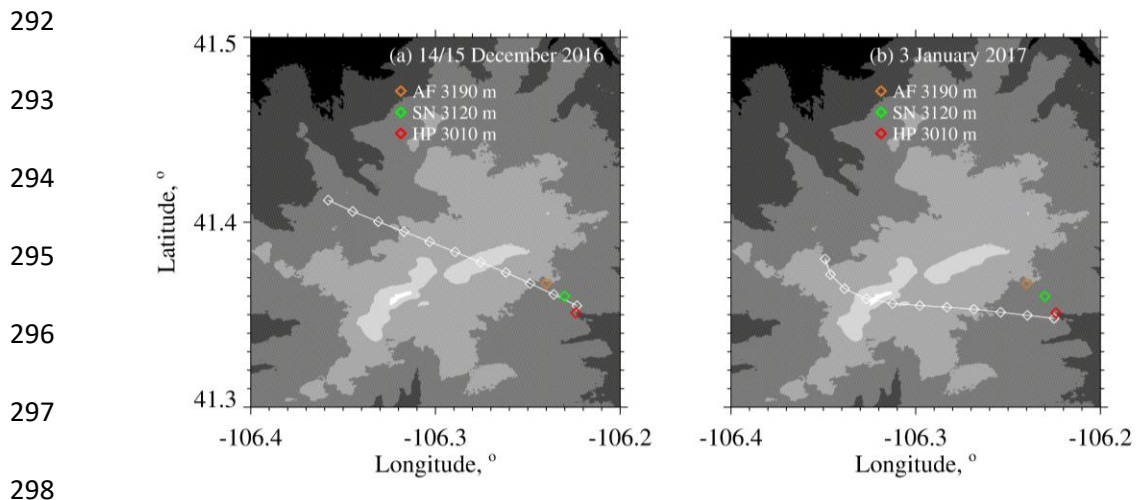
299    Figure 3 – (a) WKA flight track on 14/15 December 2016 for time interval = overflight time -

300    100 s to the overflight time. (b) WKA flight track on 3 January 2017 for time interval =

301    overflight time - 100 s to the overflight time. The white diamonds on the tracks are separated, in

302    time, by 10 s. Altitude thresholds for the digital elevation maps are 2600, 2800, 3000, 3200,

303    3400, and 3600 meters. Altitudes of the ground sites are in the legend.

304

**3.2 – Effect of Attenuation on WCR Reflectivities**

The presence of molecular oxygen, water vapor, cloud water, and snow particles within the WCR's transmission path will contribute to an attenuation of microwave intensity and will therefore negatively bias the retrieved reflectivities (Matrosov 2007; Hiley et al. 2011; Kneifel et al. 2015). Models of attenuation, radar remote sensing, and in situ measurements were used to calculate this bias. For oxygen, an attenuation coefficient from Ulaby et al. (1981; their Fig. 5.6), and temperature (T) and pressure (P) measurements from the AF (Table 3), were used. For vapor, an attenuation coefficient (Ulaby et al. 1981; their Eq. 5.22), and T, P, and relative humidity (RH) measurements from the AF (Table 3), were used. Concentrations of oxygen and water vapor and the oxygen and vapor path lengths are provided in Table 4. The latter is the vertical distance between the HP and the WKA. It was assumed that concentrations were uniform over this path length.

Attenuation by cloud water was derived using the WKA-measured T (Table 3), the WKA-measured LWC, path length (Table 4), and an attenuation formula (Liebe et al. 1989; Vali and Haimov 2001). The LWC applied in the formula is the maximum of CDP measurements acquired between $t_0$ - 10 s and $t_0$. This interval coincides with the interval the WCR's down-looking antenna was used to acquire reflectivities over the HP (Sect. 3.5). The path length for cloud water was derived as the vertical distance between cloud base [derived thermodynamically using AF measurements (Table 3)] and flight level. LWC was assumed uniform, at the maximum value, over the path length.

Snow particle mass concentration is typically reported as an ice water content (IWC, g m$^{-3}$) (Liu and Illingworth 2000). The contribution of IWC to attenuation was calculated using

328    measurements in Nemarich et. al (1988), who reported an attenuation coefficient equal to 0.9

329    dB/km per unit of IWC. Also used were retrievals of IWC acquired using the down-pointing

330    WCR antenna. There are several steps in the calculation. First, all profiles of dBZ acquired

331    between $t_0$ - 10 s and $t_0$ were selected. Second, a maximum dBZ was selected at each of the

332    down-beam range gates (Table 2). Third, the dBZ maxima were increased by the overall two-

333    way attenuation in the final column of Table 4. Fourth, the profile of attenuation-corrected dBZ

334    was converted to a profile of attenuation-corrected Z. Fifth, a Z-to-IWC parameterization was

335    applied (IWC = $0.10 \cdot Z^{0.51}$; PV11; their Table 3). Sixth, the IWC profile was integrated, and the

336    derived ice water path was divided by the snow particle path length (Table 4). This calculation

337    produced a time- and range-averaged maximum IWC (Table 4). This IWC is the value applied in

338    the attenuation calculation.

339        Two-way attenuations ($\Delta dB$), summed over contributions from the four components, are

340    presented in the final column of Table 4. Attenuation by snow and attenuation by liquid were the

341    most important components (> 50 %) on December 15 and January 3, respectively. Vapor

342    contributed 32 % to the overall on December 15, and the combination of vapor and snow

343    contributed 45 % on January 3. Equation 1 shows how an attenuation-corrected reflectivity ($Z'$)

344    was derived using an uncorrected reflectivity ($Z$) and the $\Delta dB$.

345

346        $$Z' = 10^{\left[\left[10 \cdot \log_{10}(Z) + \Delta dB\right]/10\right]} \quad\quad\quad\quad\quad\quad (1)$$

347 Table 3 – Atmospheric state averages

348

| Date | WKA [a] Track Altitude, m | WKA [a] T, °C | AF [b] T, °C | AF [b] RH, % | WKA [a, c] Track Vector | WKA [a, c] Wind Vector | AF [b, c] Wind Vector |
|---|---|---|---|---|---|---|---|
| 14/15 December 2016 | 4546 | -13.9 | -6.3 | 86 | 310 / 130 | 274 / 32 | 250 / 8.5 |
| 3 January 2017 | 4196 | -21.7 | -14.6 | 77 | 280 / 120 | 265 / 27 | 260 / 5.4 |

349
350

351 [a] Altitude, temperature, track vector, and horizontal wind vector data obtained by averaging 1 Hz

352 WKA measurements. The averaging interval is 60 s and the interval starts at the overflight time,

353 minus 60 s, and ends at the overflight time.

354

355 [b] Temperature (T), relative humidity (RH), and horizontal wind vector data from sensors on the

356 US-GLE AmeriFlux tower (Sect. 2.1). The wind sensor was deployed at 26 m AGL (3223 m

357 MSL) and the T/RH sensor was deployed at 23 m AGL (3220 m MSL). The AF measurements

358 correspond to 30-minute averages closest to the overpass time. In the AF data set, time stamps on

359 the relevant AF recordings are 00:00 UTC (15 December 2016) and 20:30 UTC (3 January

360 2017).

361

362 [c] Vectors are presented in the following format: Direction of motion (degree relative to true

363 north) / speed (m s$^{-1}$).

364    Table 4 – Attenuating component concentration, one-way pathlength, and the overall two-way attenuation

| Date | Conc. Oxygen, kg m$^{-3}$ | Conc. Vapor, kg m$^{-3}$ | Maximum LWC, g m$^{-3}$ | Maximum IWC, g m$^{-3}$ | One-way Pathlength [a] Oxygen, Vapor, and Snow, km | One-way Pathlength [b] Cloud Water, km | Overall Two-way Attenuation, ΔdB |
|---|---|---|---|---|---|---|---|
| 15 December 2016 | 0.21 | 2.7x10$^{-3}$ | 0.01 | 0.27 | 1.54 | 1.09 | 1.41 [c] |
| 3 January 2017 | 0.21 | 1.3x10$^{-3}$ | 0.08 | 0.09 | 1.19 | 0.59 | 1.01 [d] |

365

366    [a] Vertical distance between HP and WKA

367

368    [b] Vertical distance between cloud base [derived thermodynamically using AF measurements (Table 3)] and WKA

369

370    [c] One-way attenuation coefficients are 0.03 dB/km for oxygen (Ulaby et al. 1981), 0.14 dB/km for vapor (Ulaby et al. 1981), 0.056

371    dB/km for cloud water (Liebe et al. 1989; Vali and Haimov 2001), and 0.24 dB/km for snow particles (Nemarich et al 1988).

372

373    [d] One-way attenuation coefficients are 0.03 dB/km for oxygen (Ulaby et al. 1981), 0.073 dB/km for vapor (Ulaby et al. 1981), 0.49

374    dB/km for cloud water (Liebe et al. 1989; Vali and Haimov 2001), and 0.077 dB/km for snow particles (Nemarich et. al 1988).

375

376 **3.3 - Correction of Doppler Velocity**

377       We accounted for bias in $V_D$ (Sect. 2.3) due to deviation of the down-looking WCR

378 antenna from vertical. This was done by applying the correction described in Zaremba et al.

379 (2022) (their Eq. A4). The west-to-east and south-to-north particle velocities used in the

380 correction were assumed to be equal to component wind velocities. The latter were expressed as

381 linear functions of altitude using the information in the penultimate and last columns of Table 3.

382 The component velocities as functions of altitude and the linear equations relating velocity and

383 altitude are provided in the Appendix.

384 **3.4 - Hotplate Measurement of Wind Speed**

385       Here we compare the hotplate-derived wind speed to wind speed derived using an

386 R.M.Young rotating anemometer (R.M.Young 2001). The second of these is symbolized $U_{RMY}$

387 and the basis for the first ($U_{PRO}$) is a proprietary algorithm (Sect. 2.4). We are doing this

388 comparison because B14 showed that $U_{PRO}$ can be high-biased, relative to a conventional

389 anemometer, and because $U_{PRO}$ is the primary determinant of the rate that the up-viewing plate

390 dissipates sensible heat energy. Diagnosis of that heat transfer rate is our basis for calculating the

391 liquid-equivalent snowfall rate (Z18). The $U_{PRO}$ also determines the snow particle catch

392 efficiency and the latter was used in calculations of the undercatch-corrected liquid-equivalent

393 snowfall rate (Sect. 2.4).

394       The comparisons reported here were done at the Laramie, WY Airport in December

395 2019, and in January 2020. Compared to the HP site, the Laramie Airport site (indicated LA in

396 Fig. 1) is free of obstruction, out to 120 m, and experiences larger wind speeds. By mounting the

397 hotplate and the R.M.Young anemometer on rigid metal pipes, the hotplate's heated horizontal

398     surfaces (the up- and down-viewing plates seen in Fig. 1 of Z18) and the anemometer's spinning

399     axis (oriented horizontally) were both positioned at 2 m AGL. The pipes were separated

400     horizontally by 5 m. There was no precipitation on the days selected for the wind speed

401     comparisons. The values of $U_{PRO}$ and $U_{RMY}$ we analyzed were recorded with a data system that

402     time stamped the 1 Hz $U_{PRO}$ and 1 Hz $U_{RMY}$ with a relative timing accuracy no worse than 1 s.

403          A wind speed comparison - from 13 December 2019 - is shown in Fig. 4a. $U_{PRO}$ was

404     brought into the comparison by sampling it once per minute from files containing 1 Hz

405     recordings of the one-minute running-average $U_{PRO}$ (Sect. 2.4). $U_{RMY}$ was brought into the

406     comparison by starting with files containing 1 Hz recordings and converting these to one-minute

407     averages. Fig. 4a shows no evidence of bias and Fig. 4b demonstrates that the average absolute

408     departure between the $U_{PRO}$ and $U_{RMY}$ (both one-minute averages) is no larger than 1 m s$^{-1}$. Table

409     5 has eight more precipitation-free comparisons. Included in the table are temperature and wind

410     speed averaged over the comparison intervals (4 to 20 UTC), the slope of the linear-least-squares

411     fit line (forced through the origin, red line), and the lower and upper quartiles of the slope. The

412     quartiles were calculated using the method of Wolfe and Snider (2012). In contrast to Figs. 4a-b,

413     Figs. 4c-d make the comparison using 1 Hz values of $U_{PRO}$ and $U_{RMY}$. The larger scatter and

414     larger average absolute departure seen in these panels is a consequence of the hotplate's limited

415     time response, compared to the R.M.Young. We quantify the hotplate's response time in terms of

416     a calculated thermal response time. During wintertime at the Laramie Airport, and with wind

417     speed at 5 m s$^{-1}$, the down-viewing plate's thermal response time is approximately 60 s (results

418     not shown). Because the temperature of the down-viewing plate is actively controlled, this does

419     not translate to a 60 s lag between changes in wind speed and the hotplate response. The

420     $U_{PRO}/U_{RMY}$ departure is most evident at $U_{PRO} > 5$ m s$^{-1}$ (Fig. 4d) but this is not a concern for

421     $U_{PRO}$ on 14/15 December 2016 or on 3 January 2017. Snider (2023) demonstrated that the $U_{PRO}$

422     was less than 5 m s$^{-1}$ at the hotplate during the two WKA overflights.
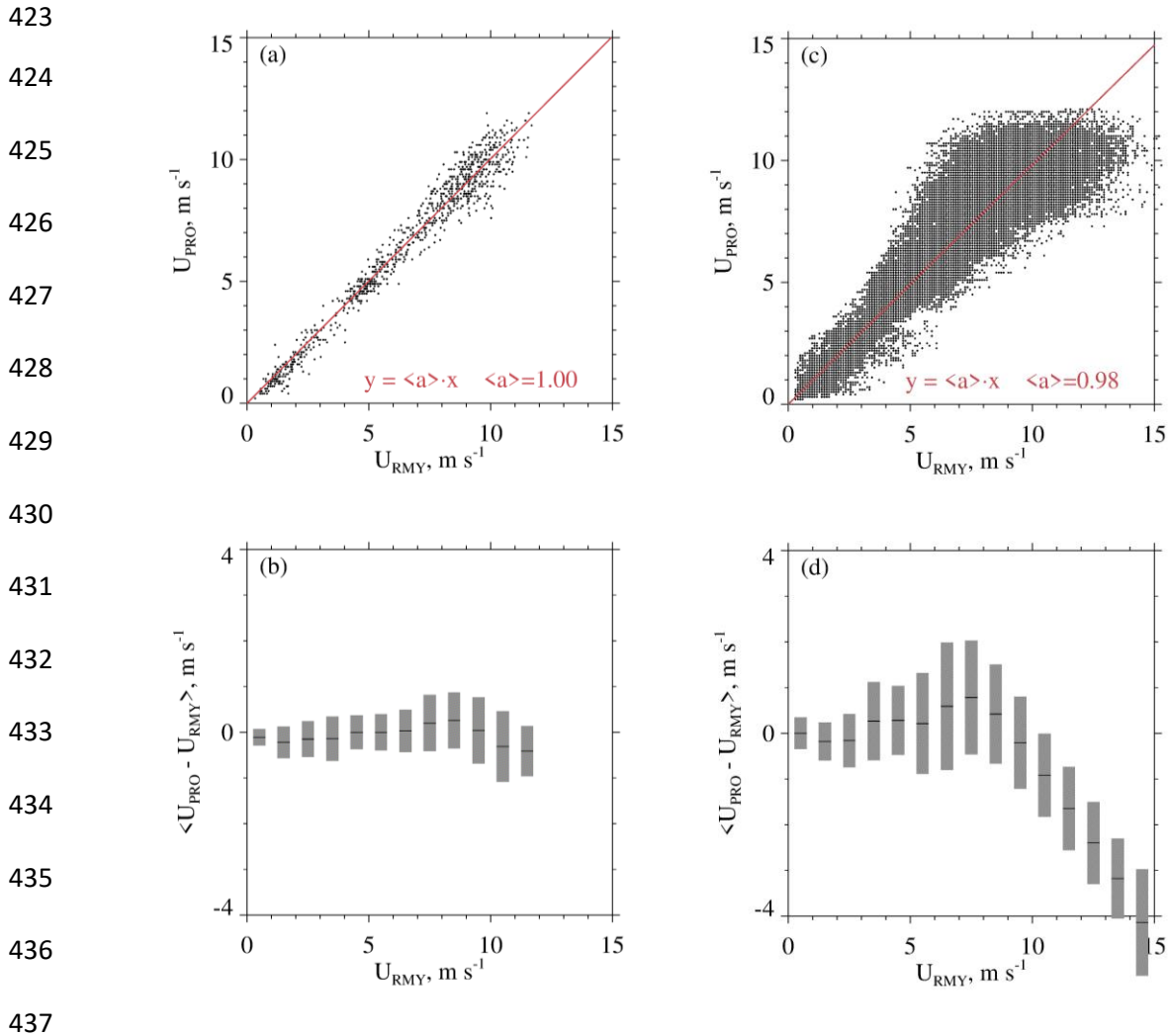
Figure 4 – (a) Scatterplot of one-minute-averaged $U_{PRO}$ and one-minute-averaged $U_{RMY}$. Measurements were acquired at the Laramie, WY Airport 13 December 2019. The red line is a linear-least-squares fit line (forced through the origin). (b) Average departure between one-minute-averaged $U_{PRO}$ and one-minute-averaged $U_{RMY}$. Average departures were calculated for discrete $U_{RMY}$ intervals, and the averages are indicated with short black horizontal lines. Gray bars indicate $\pm$ 1 standard deviation. (c) Same as in (a) except for 1 Hz values of $U_{PRO}$ and $U_{RMY}$. (d) Same as in (b) except for 1 Hz values of $U_{PRO}$ and $U_{RMY}$.

446
447 Table 5 - $U_{PRO}$ versus $U_{RMY}$ correlations

448

| Date, UTC [1] | $\langle T \rangle$ [2], °C | $\langle U \rangle$ [2], m s$^{-1}$ | $\langle a \rangle$ [3] | a [4] First Quartile | a [4] Third Quartile |
|---|---|---|---|---|---|
| 7 December 2019 | -0.40 | 5.40 | 1.00 | 0.90 | 1.04 |
| 8 December 2019 | 2.70 | 4.10 | 0.99 | 0.90 | 1.04 |
| 10 December 2019 | -5.20 | 3.80 | 0.99 | 0.83 | 1.04 |
| 13 December 2019 | -1.50 | 6.60 | 1.00 | 0.93 | 1.06 |
| 18 December 2019 | -6.20 | 3.60 | 0.99 | 0.92 | 1.04 |
| 19 December 2019 | -6.90 | 2.70 | 0.95 | 0.84 | 0.99 |
| 6 January 2020 | -6.40 | 8.80 | 1.01 | 0.96 | 1.06 |
| 8 January 2020 | 0.30 | 4.20 | 1.00 | 0.87 | 1.05 |
| 11 January 2020 | -7.20 | 7.00 | 1.02 | 0.97 | 1.08 |

449
450

451 [1] Statistics presented are based on one-minute-averaged $U_{PRO}$ and one-minute-averaged $U_{RMY}$

452 measurements made between 04:00 to 20:00 UTC.

453

454 [2] Interval-averaged temperature and interval-averaged wind speed.

455

456 [3] Slope of the one-minute-averaged $U_{PRO}$ versus one-minute-averaged $U_{RMY}$ linear-least-squares

457 fit line, forced through the origin.

458

459 [4] Quartiles of the slope (see text)

460

461 **3.5 – Combined Aircraft and Surface Measurements**

462   Figure 5 has WCR and WKA measurements starting 100 s prior to $t_0$ and ending at $t_0$.

463 The sequences in Figs. 5a and 5c are reflectivities from both the up- and down-looking antennas.

464 In Fig. 5a the flight track (black dashed horizontal line) is at 4550 m and in Fig. 5c the flight

465 track is at 4200 m. At the $t_0$ in Fig. 5a, below the WKA, the maximum radar echo is +6 dBZ (Z

466 = 4 $mm^6$ $m^{-3}$) and in Fig. 5c the maximum is -3 dBZ (Z = 0.5 $mm^6$ $m^{-3}$). Supercooled liquid

467 water was detected as the aircraft approached the ridgeline (Fig. 5b) and during the last 10

468 seconds of the time sequence in Fig. 5d. During these encounters with supercooled liquid, the

469 maximum LWC values were $0.03 \times 10^{-3}$ and $0.08 \times 10^{-3}$ kg $m^{-3}$ on 14 December 2016 and 3

470 January 2017, respectively. Values of N (Sect. 2.2) at times of maximal LWC were $3 \times 10^6$ and

471 $100 \times 10^6$ $m^{-3}$ on 14 December 2016 and 3 January 2017, respectively. Even on 3 January 2017,

472 the <D> (Sect. 2.2) associated with maximum LWC was sufficient for hexagonal plate crystals

473 with diameter larger than 100 μm to collide with the observed droplets with efficiencies > 0.1

474 (Wang and Ji 2000).

475   We temporally and spatially averaged the values of Z we compared with time-averaged

476 values of S. There are two reasons for this: 1) As discussed in Sect. 3.1, the WCR did not sample

477 Z exactly over the hotplate, and furthermore, the width of radar beam at 1500 m range - roughly

478 the distance between the aircraft and the ground at the overflight times - is 30 m and thus

479 considerably smaller than the minimum horizontal distance between the aircraft and the HP. 2)

480 Compared to the WCR, the hotplate is a relatively slow-response measurement system whose

481 output is commonly averaged over one-minute intervals (Z18).

482
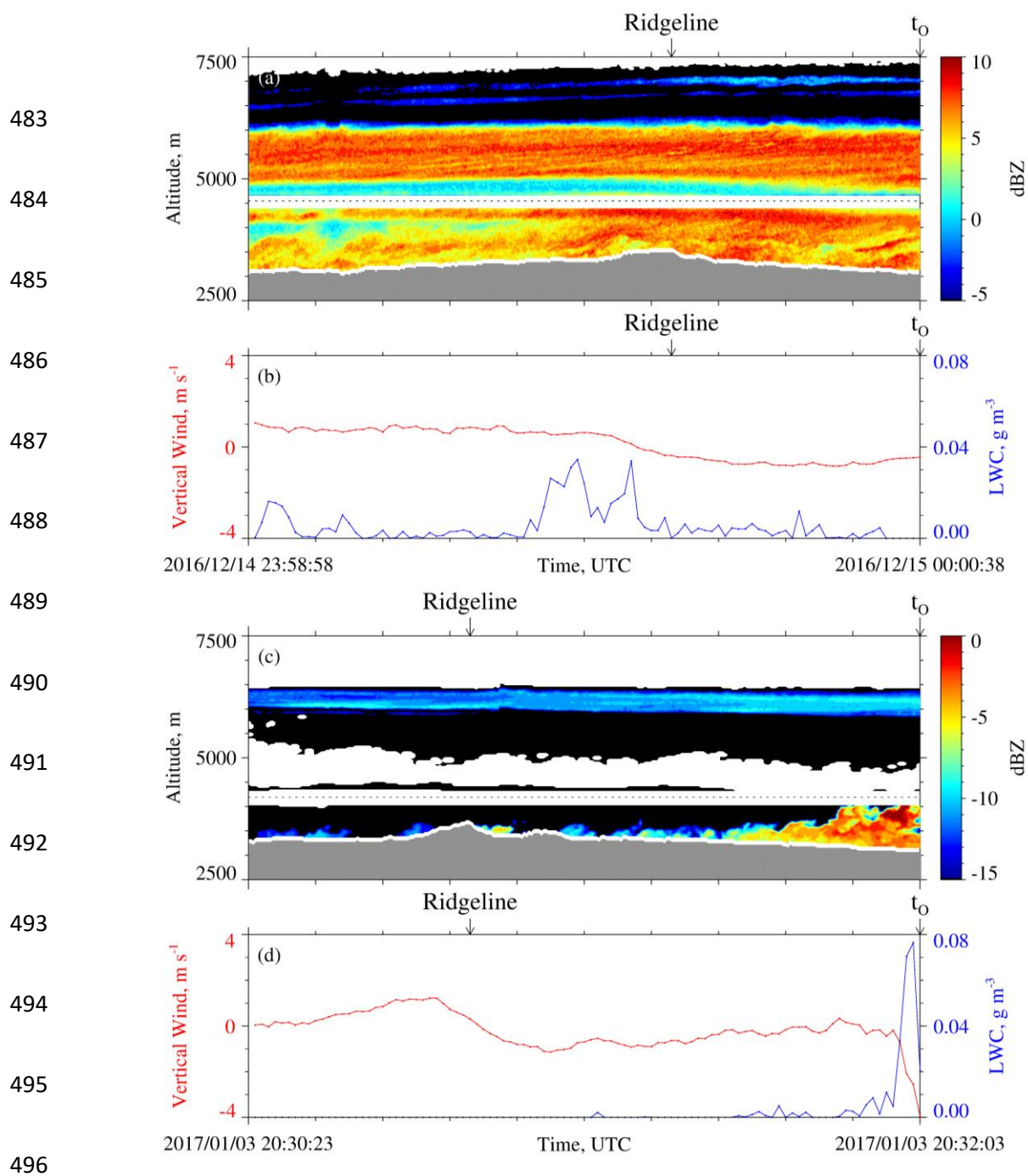
Figure 5 – (a) 100 s of WCR reflectivity and (b) 100 s of LWC and gust probe vertical

wind velocity ending at $t_0$ on 14/15 December 2016. (c) 100 s of WCR reflectivity and (d) 100 s

of LWC and gust probe vertical wind velocity ending at $t_0$ on 3 January 2017. In (a) and (c),

above and below the flight track, the roughly 200-m-deep WCR blind zone is evident,

reflectivity above (below) the flight track is from the up-looking (down-looking) WCR antenna,

502    black indicates dBZ values smaller than the minimum indicated in the color bar, white

503    immediately above the terrain indicates echo that was discarded because of ground clutter, and

504    white above the ground clutter and outside of the blind zone indicate dBZ < minimum detectable

505    signal.

506       In our analysis, the HP measurements were averaged over two adjacent 60 s intervals.

507    The first extends from $t_0$ to $t_0 + 60$ s (Fig. 6a) and the second from $t_0 + 60$ s to $t_0 + 120$ s (Fig.

508    6c). In Fig. 6a and in Fig. 6c, $t_{HP,B}$ symbolizes an interval's beginning time and $t_{HP,E}$ symbolizes

509    an interval's ending time. Formulas describing how these times were related to the beginning and

510    ending time of a corresponding WCR averaging interval are in the Appendix. Fig. 6b is a

511    schematic of the first WCR averaging interval and Fig. 6d is a schematic of the second. Again,

512    the subscripts "B" and "E" are used to indicate averaging beginning and ending times. Figures 6b

513    and 6d both have lines at the top of an averaging interval/domain. The slopes of these lines are

514    proportional to the ratio of two speeds. These speeds are a maximum likely snow particle speed

515    toward the ground ($v_p$) and a horizontal wind advection speed ($v_w$). The $v_p$ was calculated

516    using averaged vertical-component Doppler velocities and $v_w$ was calculated using a vertical

517    profile of horizontal winds, based on WKA horizontal wind measurements and AF horizontal

518    wind measurements (Figs. A1a-b), and using the WKA track vector (Table 3). An altitude ($z' =$

519    3400 m) was assumed in the calculation of $v_w$. This is the altitude of the ridges west and

520    northwest of the HP site (Figs. 3a-b). Picking the altitude to be either $z' = 3200$ m or $z' = 3600$ m

521    does not alter our findings.

522
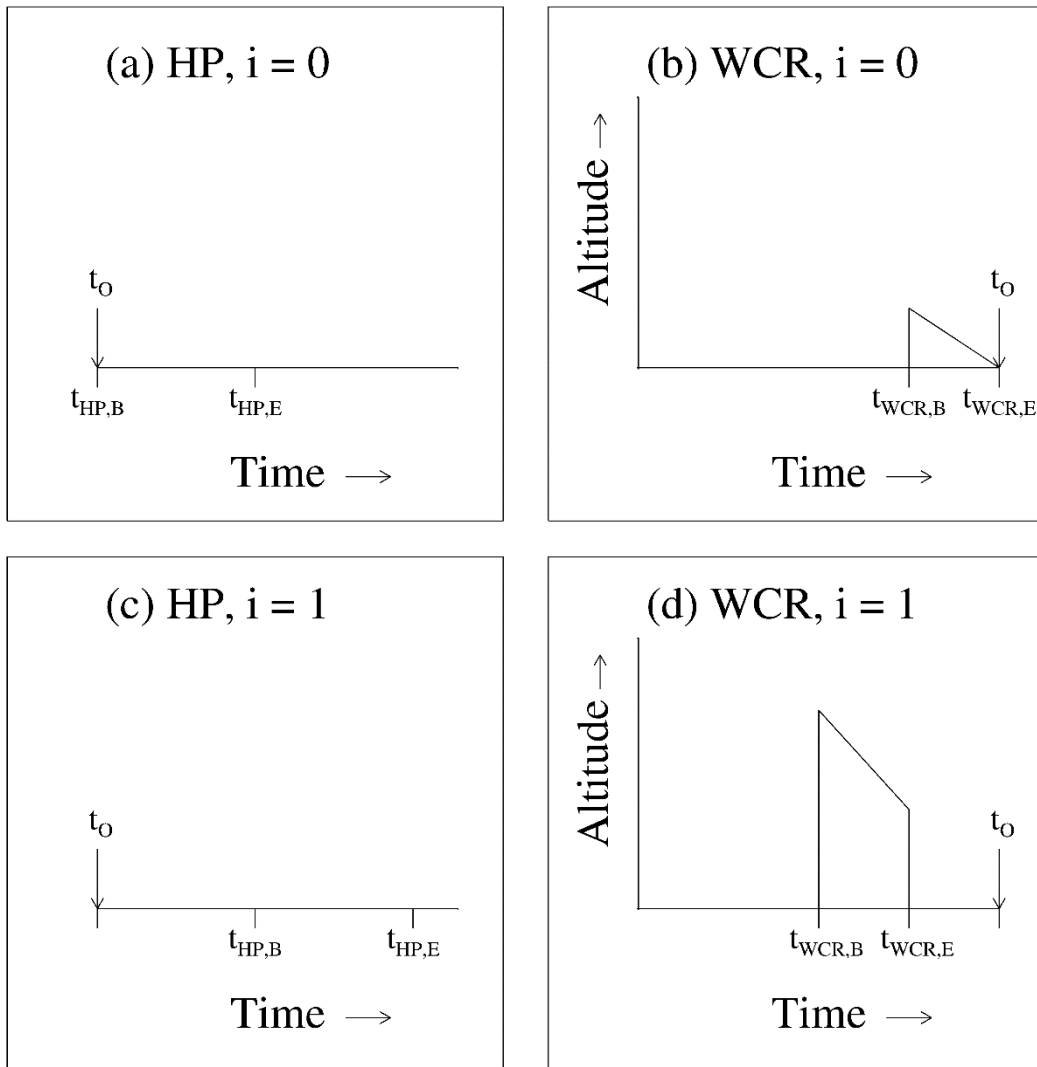
Figure 6 – (a and c) Representations of the $i = 0$ and $i = 1$ HP averaging intervals. (b and d)

Representations of the $i = 0$ and $i = 1$ WCR averaging intervals/domains. The $t_0$ is shown in all

panels. The subscripts "B" and "E" indicate beginning and ending times of the HP averaging

(panels a and c) and the beginning and ending times of the WCR averaging (panels b and d).

548

549       All panels in Fig. 6 are labeled with an index designating either the first averaging

550    interval ($i = 0$) or the second averaging interval ($i = 1$). Figures 7 and 8 present hotplate

551    snowfall measurements from 14/15 December 2016 and 3 January 2017. In these, and in

552    subsequent figures, colored circles surround the $i = 0$ and $i = 1$ indexes, blue is used to color-

553    code 15 December 2016, and red is used to color-code 3 January 2017. Additionally, Fig. 8 has

554    an $i = 2$ averaging interval. This is a special case discussed at the end of this section.

555       Figures 9a-b and Figs. 10a-b have enlarged views of the altitude-time WCR crossections

556    recorded on the two flight days. Different from Fig. 5a and Fig. 5c, these measurements are only

557    from the WCR's down-looking antenna. Additional differences are the following: 1) The plots

558    are set up so that Z and $V_D$ structures downwind of the hotplate can be seen. These structures are

559    discussed in the following section. 2) The WCR measurements are shown for 50 s of flight. With

560    the WKA ground speed approximately 125 m s$^{-1}$ (Table 3), the distance along the abscissa is

561    6250 m. 3) Colored circles that surround the indexes are placed below the WCR averaging

562    intervals/domains. The latter are drawn with solid black lines and are seen to overlay both the Z

563    and $V_D$ altitude-time crossections. Consistent with Figs. 6b and 6d, and the Appendix, one of

564    these black lines is vertical and another is negatively sloped. Figs. 10a-b also have the $i = 2$

565    intervals/domains discussed at the end of this section.
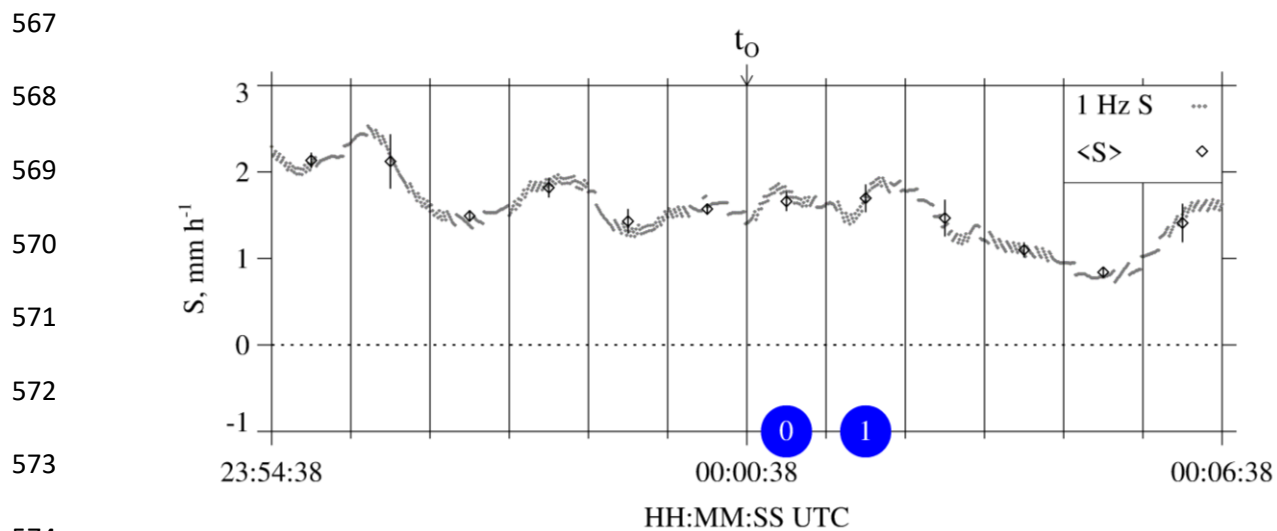
566

Figure 7 – Twelve minutes of HP snowfall measurements from 14/15 December 2016. Gray dots

are S values calculated using hotplate output recorded at 1 Hz. Black diamonds are the one-

minute-averaged values (± 1 standard deviation). The $t_0$ is shown above the panel and blue

circles designate the $i = 0$ and $i = 1$ HP averaging intervals.

581

582

583

584

585

586

587

588

589
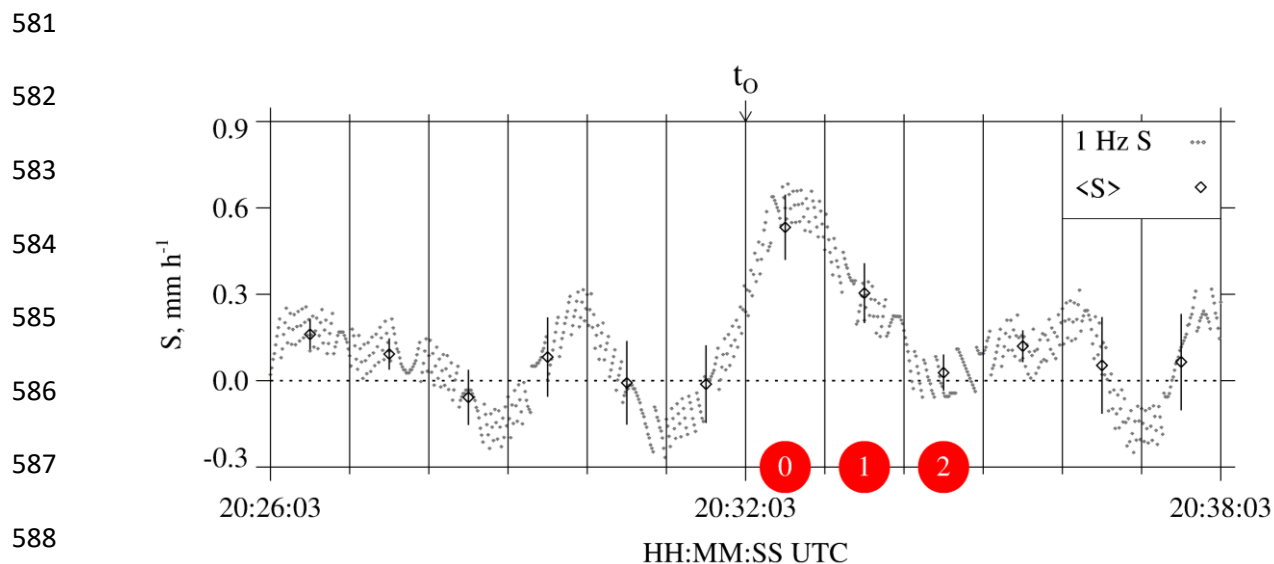
590    Figure 8 – Twelve minutes of HP snowfall measurements from 3 January 2017. Gray dots are S

591    values calculated using hotplate output recorded at 1 Hz. Black diamonds are the one-minute-

592    averaged values ($\pm$ 1 standard deviation). The $t_0$ is shown above the panel and red circles

593    designate the $i = 0$, $i = 1$, and $i = 2$ HP averaging intervals. The $i = 2$ interval is a special case

594    discussed at the end of Sect. 3.5.

595

596

597

598

599

600

601

602

603

604

605

606

607
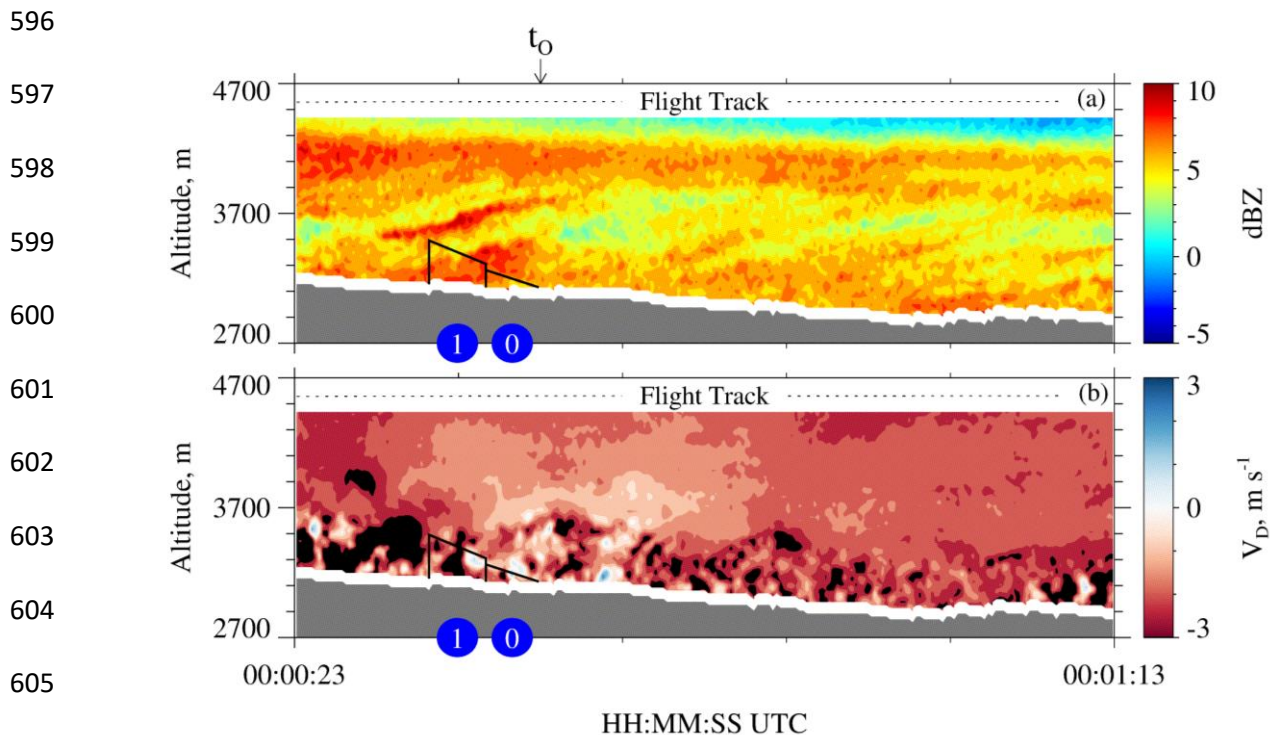
608  Figure 9 – 50 s of measurements from the down-looking WCR antenna on 15 December 2016.

609  (a) Crossection of reflectivity $t_0$ - 15 s to $t_0$ + 35 s. (b) Crossection of Doppler velocity $t_0$ - 15 s

610  to $t_0$ + 35 s. The $t_0$ is shown above the top panel. In both panels, the solid black lines (vertical

611  and sloped) encompass the $i = 0$ and $i = 1$ WCR averaging intervals/domains and blue circles

612  designate the WCR averaging intervals.

613
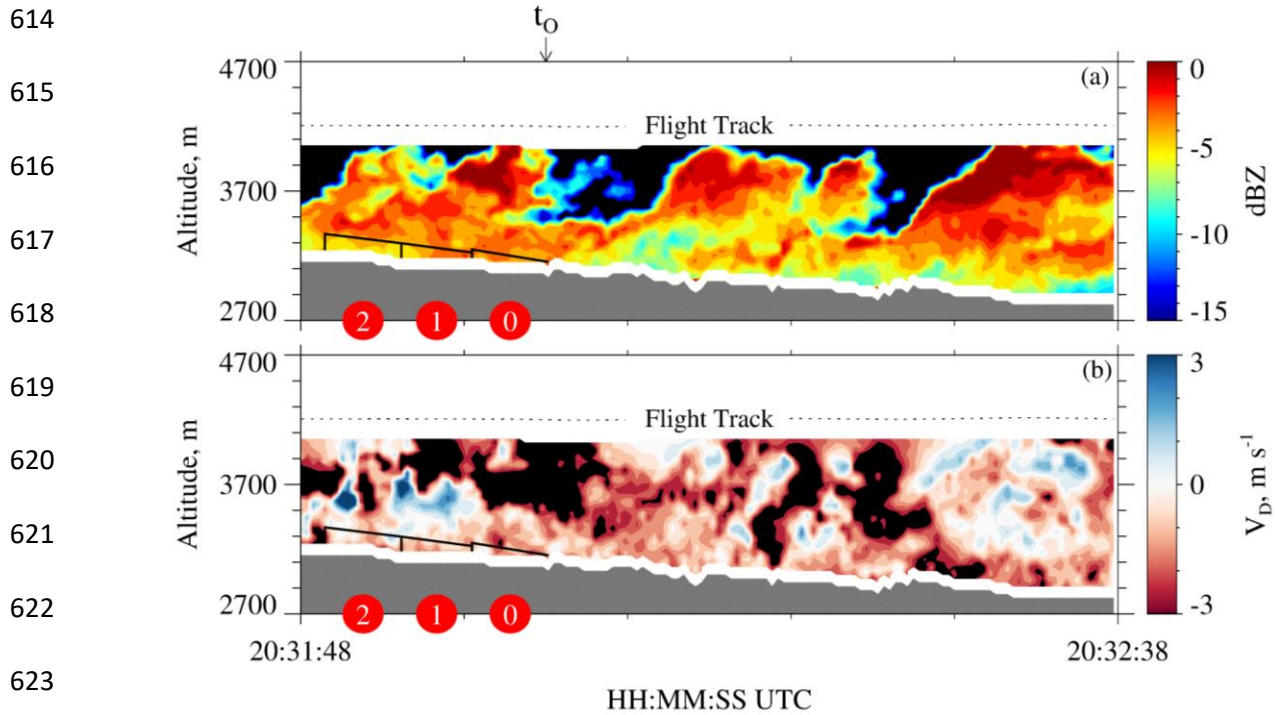
Figure 10 – 50 s of measurements from the down-looking WCR antenna on 3 January 2017. (a)

Crossection of reflectivity $t_0$ - 15 s to $t_0$ + 35 s. (b) Crossection of Doppler velocity $t_0$ - 15 s to $t_0$

+ 35 s. The $t_0$ is shown above the top panel. In both panels, the solid black lines (vertical and

sloped) encompass the $i = 0$, $i = 1$, and $i = 2$ WCR averaging intervals/domains and red circles

designate the $i = 0$, $i = 1$, and $i = 2$ WCR averaging intervals/domains. The $i = 2$ interval/domain

is a special case discussed at the end of Sect. 3.5.

633    The $i = 0$ and $i = 1$ averages of S and Z are presented in Table 6 and the corresponding

634    averaging intervals are viewable in Fig. 7 and Fig. 9a (15 December 2016) and in Fig. 8 and Fig.

635    10a (3 January 2017). According to the averaging scheme (Fig. 6), the $i = 1$ HP averaging

636    interval is time-shifted positively compared to the $i = 0$ HP averaging interval and the $i = 1$ WCR

637    averaging interval is time-shifted negatively compared of the $i = 0$ WCR averaging interval.

638    This arrangement of the averaging intervals is one way to average while also accounting for

639    wind advection of the snow particles.

640    As discussed earlier in this section, the averaging scheme initializes with 60-second

641    blocks of HP data between $t_O$ and $t_O + 120$ s. When we applied the scheme to data from 3 January

642    2017, but outside the specified time range, an inconsistency was documented. This is apparent in

643    Fig. 8, where the $t_O + 120$ s to $t_O + 180$ s interval (i.e., the $i = 2$ interval) has negligible average S,

644    while in Fig. 10, the $i = 2$ interval has a non-negligible average Z ($\sim 0.3$ mm$^6$ m$^{-3}$). A firm

645    explanation is not available for the inconsistency, but a factor may be the convective nature of

646    the fields in Figs. 10a-b. Because of the inconsistency, only averages corresponding to the $i = 0$

647    and $i = 1$ intervals are analyzed further.

648 Table 6 – Average wind measurements, average hotplate measurements, average WCR measurements, and attenuation-corrected

649 reflectivities

| Date | $v_w$ [a], m s$^{-1}$ | i index | $S_{HP} \pm \sigma$ [b], mm h$^{-1}$ | WCR Samples [c] | $<V_D>$ [d], m s$^{-1}$ | $\sigma_{V_D}$ [e], m s$^{-1}$ | $v_p$ [f], m s$^{-1}$ | $<Z> \pm \sigma_Z$ [g], mm$^6$ m$^{-3}$ | $Z'$ [h], mm$^6$ m$^{-3}$ |
|---|---|---|---|---|---|---|---|---|---|
| 15 December 2016 | 7.4 | 0 | 1.7±0.1 | 42 | -1.3 | 0.9 | 2.2 | 4.9±2.1 | 6.8 |
| 15 December 2016 | 7.4 | 1 | 1.7±0.2 | 149 | -1.8 | 1.2 | 3.0 | 5.6±1.1 | 7.8 |
| 3 January 2017 | 8.9 | 0 | 0.5±0.1 | 22 | -0.9 | 0.8 | 1.7 | 0.49±0.05 | 0.62 |
| 3 January 2017 | 8.9 | 1 | 0.3±0.1 | 35 | -0.8 | 0.4 | 1.2 | 0.50±0.10 | 0.63 |

650

651 [a] Horizontal wind advection speed (Eq. A7) calculated using values from the penultimate and last columns of Table 3.

652 [b] One-minute average of the undercatch-corrected liquid-equivalent snowfall rate (± 1 standard deviation). An example averaging

653 interval is the $i = 0$ interval in Fig. 7.

654 [c] Number of samples used to calculate the WCR statistics. The averaging intervals/domains (e.g., $i = 0$ in Figs. 9a-b and in Figs. 10a-

655 b) encompass the WCR samples which are the basis for the WCR statistics presented in this table.

656 [d] Average of Doppler velocity within the averaging intervals/domains.

657 [e] Standard deviation of Doppler velocity within the averaging intervals/domains.

658 [f] Maximum likely snow particle speed toward the ground (Eq. A8).

659 [g] Average reflectivity (± 1 standard deviation). These values are not corrected for attenuation.

660 [h] Attenuation-corrected reflectivities. These were derived using reflectivities from the penultimate column of this table, attenuations

661 from Table 4, and Eq. 1.

### 3.6 - Snow Particle Imagery

In Fig. 9a and Fig. 10a, the time for a snow particle to move the abscissa and ordinate distances is different. The ratio of these two times is 2.6. This follows from our choice of abscissa and ordinate ranges, from values of particle fall speed (1 m s$^{-1}$) and horizontal wind advection speed (8 m s$^{-1}$), which we assumed, and from the WKA ground speed ( $gs \sim 125$ m s$^{-1}$; Table 3). The assumed values are approximately consistent with values of $<V_D>$ and $v_w$, in Table 6, and with the $V_D$ sign convention (Sect. 2.3). We also used $gs = 125$ m s$^{-1}$ to scale (virtually) the time axes in Fig. 9a and Fig. 10a to a horizontal distance. Within the scaled coordinate frames, we assumed that all snow particle trajectories have negative slope ($\Delta z / \Delta x = -$ 1 m s$^{-1}$ / 8 m s$^{-1}$ = -0.12) and that all trajectories are stationary. However, both assumptions seem inconsistent with the reflectivity structures in Fig. 5a, where positively-sloped particle fall streaks are evident at ~ 5500 m, inconsistent with Fig. 9a where positively-sloped fall streaks are at ~ 3500 m, and inconsistent with the positively-sloped fall streaks in Fig. 10a. On both flight days, the fall streaks evince particle sources that move horizontally and with a horizontal speed that is larger than the $v_w = 8$ m s$^{-1}$ applied in the estimate of the trajectory slope. It may be that the source's horizontal speed is comparable to the flight-level WKA-derived horizontal wind (27 to 32 m s$^{-1}$; Table 3) but we do not have data needed to verify that assertion. Based on the assumption that snow particles followed the fall streaks while both were advecting horizontally, we looked *downwind* of the hotplate - at a time later than $t_0$ in Fig. 9a and Fig. 10a - for particles that became those that produced snowfall at the hotplate.

Particle images from 15 December 2016 were analyzed using the 2DP. With this instrument the maximum all-in particle size (in the horizontal direction perpendicular to flight) is

684    6400 μm and the particle size resolution is 200 μm (Sect. 2.2). Within the time interval picked

685    for this analysis (discussed below), particles sizing in the smaller of the two spectral modes, with

686    mode size ~ 400 μm, were more numerous (results not shown). Because the 400 μm particles are

687    poorly resolved by the 2DP, and the same can be said for somewhat larger particles, those

688    smaller than 1000 μm were excluded from the following analysis. Figure 11a shows imagery

689    from 12 s of measurements acquired near the end of the sequence in Fig. 9a (00:01:02 to

690    00:01:14). This time interval was selected by tracing forward from $t_0$, along the slope of the fall

691    streaks, to the flight level. Many of the particles are rounded (indicating riming) and a few have

692    arms likely due to incomplete conversion of branched crystals to rimed snow particles. The mode

693    size corresponding to these images is 1600 μm. No liquid water was detected with these particles

694    (LWC $< 0.01 \times 10^{-3}$ kg m$^{-3}$; Fuller 2020; her Fig. 8), but liquid was detected, at ~ 00:00:00, as the

695    aircraft approached the ridgeline (Figs. 5a-b).

696         Turning to imagery from 3 January 2017, the most appropriate location for analysis

697    would be through the second billow structure evident in Fig. 10a (i.e., very close to the middle of

698    the Fig. 10a sequence). This billow sourced a fall streak that terminated at the hotplate (i.e., at

699    the time $t_0$ indicated in the figure). However, the aircraft only clipped the top of this billow, and

700    it was only when sampling the billow seen ~ 13 s earlier that larger ice particle concentrations (~

701    20,000 m$^{-3}$) (Fuller 2020; her Fig. 10) and larger LWC (~ $0.08 \times 10^{-3}$ kg m$^{-3}$; Fig. 5d) were

702    detected. Maximum reflectivities were the same in all three billows (Z ~ 1 mm$^6$ m$^{-3}$; 0 dBZ), so it

703    was assumed that imagery collected in the first billow (20:32:00 to 20:32:02) was representative

704    of what was falling toward the hotplate. The 2DS was used to image these particles (Fig. 11b);

705    with this instrument the maximum all-in particle size (in the horizontal direction perpendicular to

706    flight) is 1280 μm and the size resolution is 10 μm (Sect. 2.2). Most of the objects in Fig. 11b

707     appear to be rimed and their mode size is ~ 400 μm. It is also noted that particles smaller than

708     100 μm were eliminated from these images, however, compared to the ~ 400 μm particles those

709     smaller than 100 μm were significantly less abundant (results not shown).

710

711    (a)

718    (b)
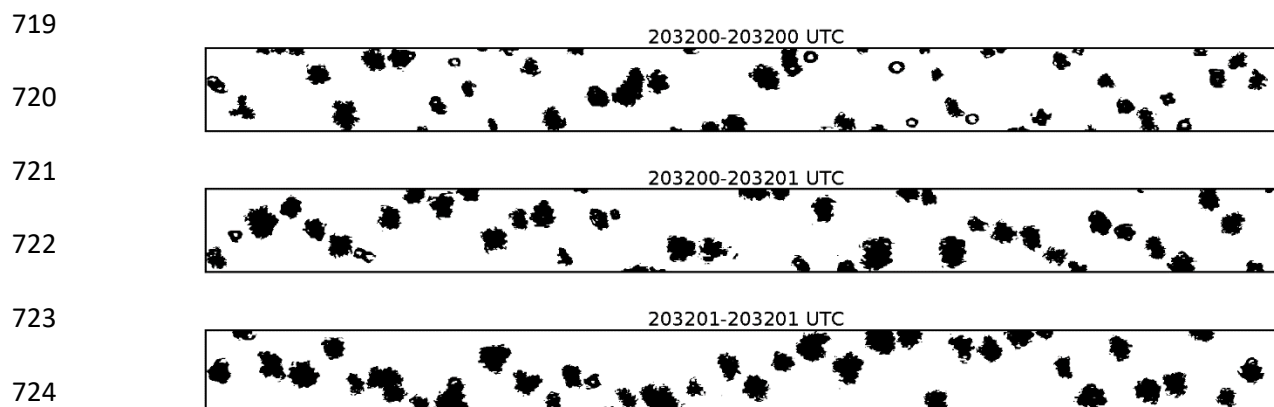
726    Figure 11 – (a) 2DP particle imagery from 15 December 2016. The height of the strips is 6400

727    μm. These particles are estimated to be representative of those that fell from flight level toward

728    the hotplate. (b) 2DS particle imagery from 3 January 2017. The height of the strips is 1280 μm.

729    These particles are estimated to be representative of those that fell from flight level toward the

730    hotplate.

731

732  **3.7 – S/Z Relationships**

733      Our S/Z pairs are presented in Table 6 where the indexes ($i = 0$ and $i = 1$) are used to

734  indicate results derived for the averaging intervals. In the penultimate column of Table 6,

735  reflectivities are not corrected for attenuation, however, in the last column of Table 6 and in Fig.

736  12, the attenuation-corrected reflectivities are presented. Reflectivities from the penultimate

737  column of Table 6, attenuations from Table 4, and Eq. 1 were used to calculate the corrected

738  reflectivities. Also shown in Fig. 12 (black filled circles) is a subset of the S/Z pairs from PV11's

739  Fig. 11 ($0.01 < Z < 10$ mm$^6$ mm$^{-3}$) and the PV11 best-fit line (black). Results from PV11 are

740  specified as $S(\rho_1)/Z$ because those authors applied the lower of two density-size functions ($\rho_1$),

741  and the lower of two fall speed-size functions, with airborne measurements, in calculations of

742  snowfall rates (Sect. 1 and Table 1).
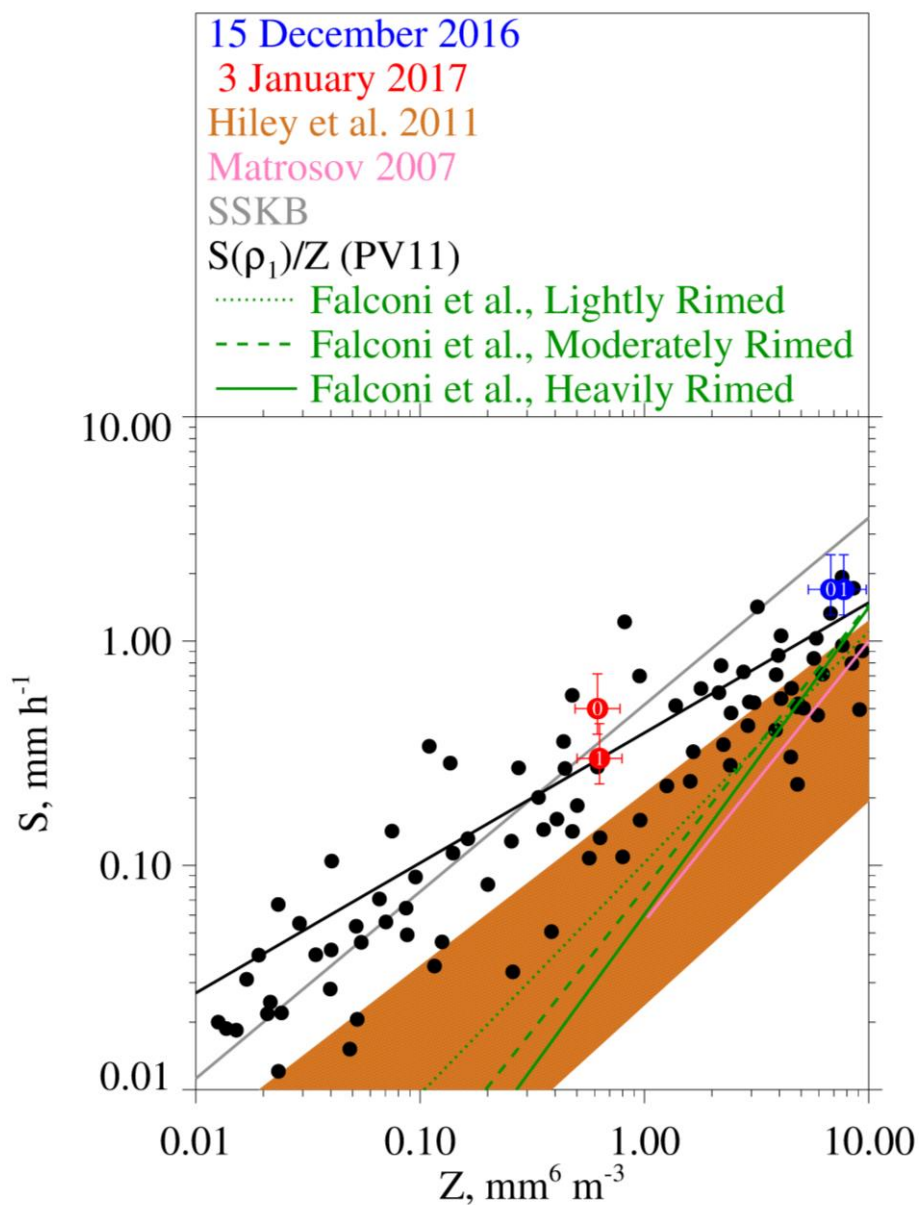
Figure 12 – Snowfall rate versus radar reflectivity. Red and blue circles are plotted at

attenuation-corrected reflectivities (Table 6) for the $i = 0$ and $i = 1$ averaging intervals. Error

bars on these points represent precisions of the reflectivity (Sect. 2.3) and snowfall rate (Sect.

2.4) measurements. Also plotted are the S/Z relationship lines from Sect. 1 and Table 1. These

are the S/Z lines defining the swath of S/Z relationships from Hiley et al. (2011), the S/Z

relationship from Matrosov (2007), the S/Z relationship abbreviated SSKB, PV11's best-fit line,

766 and the S/Z relationships from Falconi et al. (2018) (their Table 2). The $S(\rho_1)/Z$ points (black

767 filled circles) are a subset from PV11's Fig. 11 ($0.01 < Z < 10$ mm$^6$ mm$^{-3}$).

768        There are two potential biases in the values of snowfall rate we tabulate (Table 6) and

769    plot (Fig. 12). First, the two snowfall events had flight-level vertical wind velocities (Figs. 5b

770    and 5d) that were positive (upward) upwind of the ridgeline, and vice versa downwind of the

771    ridgeline. Except for the strongest downdraft on 3 January 2017, the magnitude of this variance

772    is ~ 1 m s$^{-1}$ (Figs. 5b and 5d). Assuming 1 m s$^{-1}$ was the downward wind immediately over the

773    hotplate, the snow particles would have approached the HP gauge faster than their fall speed.

774    Our basis for stating this is fall speeds for the mode sizes discussed in Sect. 3.6 (1600 and 400

775    μm) and our assumption that the particles were graupel. (Table 7 has these characteristic sizes

776    and fall speeds.) However, the conjectured relative effect of a downward wind is likely an

777    overestimate - because of divergence occurring as downward moving air approached the surface

778    - and because the sizes in Table 7 likely underestimate what fell to the hotplate. Relevant to the

779    last of these assertions, we used the altitude/T/RH measurements (Table 3) to calculate the

780    vertical distance available for growth via riming, and thus for a fall speed increase, between the

781    flight level and the lifted condensation level. Assuming an adiabatically-stratified liquid cloud

782    and unit collection efficiency (these assumptions overestimate growth by riming), and no change

783    of particle crossection (underestimates growth by riming), our calculations indicate that relative

784    increases of size and fall speed were 40 and 20 %, respectively, on 3 January 2017, and that

785    these relative increases were a factor-of-two larger on 15 December 2016.

786

787      Table 7 – Estimates of snow particle fall speed

| Date | Mode Size, μm | Assumed Particle Type | Fall Speed, m s$^{-1}$ | Reference |
|---|---|---|---|---|
| 15 December 2016 | 1600 | graupel | 1.4 | PV11; assuming $\rho_1$ in their Fig. 5 |
| 3 January 2017 | 400 | graupel | 0.7 | PV11; assuming $\rho_1$ in their Fig. 5 |

788

789

790         Second, there is concern that values of S from 3 January 2017 are underestimated.

791     Although values of S must be > 0, we presented 1 Hz values (gray points, Fig. 8) approaching -

792     0.3 mm h$^{-1}$. Negative values resulted because we did not impose a threshold of 0 mm h$^{-1}$ on the

793     uncorrected snowfall rates (this thresholding is discussed in Z18) and because negative snowfall

794     rate values (uncorrected for catch inefficiency) are amplified by the gauge-catch correction (Sect.

795     2.4). The implication is that 0.2 mm h$^{-1}$ could be added to the one-minute averaged values of

796     snowfall rate in Table 6 and in Fig. 12. Here, the assumption is that an averaged S of -0.2 mm h$^{-}$

797     $^{1}$, in Fig. 8, indicates no snowfall at the hotplate; however, because the hotplate was operated

798     autonomously (Sect. 2.1) we have no way to verify the assumption.

799

## 4 – Results

800

801     Figure 12 shows our four snowfall rate/reflectivity pairs (red and blue circles) after the

802     reflectivities were corrected for attenuation. The error bars on these data pairs represent the

803     precision of the Z measurement (Sect. 2.3) and the precision of the S measurement (Sect. 2.4).

804     Presentation clarity was what guided the selection of S and Z axis ranges in this figure but with

805     the consequence that 32 of PV11's S/Z pairs are not shown because they plot at $Z > 10$ mm$^6$ m$^{-3}$.

806     The way that the PV11 data pairs scatter closest to $Z = 10$ mm$^6$ m$^{-3}$, combined with the fact that

807     the PV11 data pairs at $Z > 10$ mm$^6$ m$^{-3}$ are not shown, could lead to the interpretation that the

808     slope describing the best-fit relationship, at Z approximately $> 2$ mm$^6$ m$^{-3}$, should be decreased

809     relative to the actual slope of the PV11 best-fit line. Readers who view PV11's Fig. 11 will

810     conclude that this interpretation is not warranted.

811     As is discussed in Sect. 1, computation-based S/Z relationship have inputs from

812     parameterized descriptions of density, shape, fall speed, PSD, and particle size. The

813     computation-based S/Z relationships are in the top three rows of Table 1; the subsequent two

814     rows of the table have S/Z relationships that resulted from a hybridization of measurements and

815     calculations (PV11 and Falconi et al. 2018).

816     We now compare our snowfall rates (fourth column of Table 6) to snowfall rates where

817     they plot on an S/Z relationship line evaluated at one of our attenuation-corrected reflectivities.

818     The departure between these is reported as a relative S difference expressed as $|(S_{HP}-S)|/S$ where

819     $S_{HP}$ is from Table 6 and where S is on an S/Z relationship line. All possible comparisons are

820     presented graphically in Fig. 12. Table 1 has both the minimum relative S differences and the

821     salient maximum relative S differences. The comparisons will be discussed in the order of

822     presentation in Table 1.

823       In comparisons of our snowfall rates and the upper-limit S/Z relationship line from Hiley

824    et al. (2011) the relative difference is no smaller than 0.7 and 1.0 on 15 December and 3 January,

825    respectively. These minimum relative differences exceed the hotplate precision (Sect. 2.4) by at

826    least a factor of two. It is concluded that our paired values of undercatch-corrected precipitation

827    rate and attenuation-corrected radar reflectivity provide evidence that a calculation of S based on

828    the Hiley et al. (2011) upper-limit, when applied to rimed snow particles, is associated with a

829    low-biased estimate of S. A retrieval based on Hiley et al.'s average S/Z relationship (not

830    shown), which bisects the orange region in Fig. 12, corresponds to an even larger low bias. This

831    is a concern because Hiley et al. (2011) used their average S/Z relationship to retrieve global

832    snowfall distributions and since global observations reported in Wang et al. (2013) document the

833    frequent occurrence of supercooled liquid within snowing clouds.

834       Figure 12 shows the separation between our measurements and the Matrosov (2007)

835    calculation. The separation is about a factor of two (minimum relative difference = 1.4) for the

836    points obtained on 15 December 2016 and corresponds to an underestimation of S (low bias)

837    when compared to our measurements. The points from 3 January 2017 plot at an attenuation-

838    corrected reflectivity smaller than the lower-limit of the calculation (Matrosov 2007). Since the

839    particle images (Fig. 11a-b) reveal no evidence of the particle type modeled by Matrosov (2007)

840    (aggregates), it is not surprising that the Matrosov S/Z relationship is not representative of our

841    measurements.

842       One plausible reason for the low bias discussed in the previous two paragraphs is the

843    smaller density implicit in most computationally-based S/Z relationships and especially those

844    which assume that snow particles are crystals. Densities are quite different for crystals versus

845    that for rimed snow particles. For example, in Brown and Francis (1995), assuming a 2 mm

846    crystal, the density is ~ 30 kg m$^{-3}$, whereas in PV11 (their Eq. 1), assuming a 2 mm graupel

847    particle, the density is ~ 200 kg m$^{-3}$. Because aggregates are collections of crystals, this

848    comparison of crystal and graupel densities also seems relevant to a comparison of graupel and

849    aggregate snow particle densities.

850        Figure 12 compares our $S_{HP}/Z'$ data pairs to the SSKB S/Z relationship line and Table 1

851    presents the relative differences between the data pairs and the SSKB line. Compared to the S/Z

852    relationship represented by top of the orange region in Fig. 12, and compared to the Matrosov

853    2007 relationship, the SSKB line plots closer to our data points (minimum relative difference ~

854    0.3). We note that the only instances of $S_{HP} < S$ are three of four comparisons of our

855    measurements to the SSKB relationship. A possible reason for this is that the density applied in

856    SSKB (Table 1) is not entirely representative of conditions during our study. An analysis of the

857    sensitivity of the SSKB to a change in density is needed to investigate our assertion.

858        Comparisons of our $S_{HP}/Z'$ data pairs and PV11's best-fit line are also in Table 1. The

859    table demonstrates that the agreement is reasonable - minimum relative difference no larger than

860    0.3 – and Fig. 12 shows that our data pairs plot at or above the PV11 best fit line.

861        Based on data from PV11 and our $S_{HP}/Z'$ data pairs, as well as the S/Z relationship

862    abbreviated SSKB, it is expected that the S/Z relationships reported by Falconi et al. (2018) for

863    rimed snow particles (Sect. 1) would plot higher in S-versus-Z space than is illustrated in Fig. 12.

864    Notably, only the upper-end of the Falconi et al. lines (i.e., at Z > 8 mm$^6$ m$^{-3}$) plot above the

865    upper-limit that Hiley et al. (2011) developed for unrimed snow particles. A plausible

866    explanation for the lower-than-expected S/Z relationships of Falconi et al. is now offered.

867    Falconi et al. used liquid water path as a proxy for the extent of snow particle riming (von Lerber

868    et al. 2017). A consequence may have been that the proxy did not dependably exclude unrimed

869    snow particles (crystals and aggregates) from the riming categories of Falconi et al. If this was

870    the case, then the data groupings that were the basis for the Falconi et al. S/Z relationships may

871    have been affected. When comparing the heavily-rimed S/Z relationship of Falconi et al. to our

872    $S_{HP}/Z'$ data pairs we find that the minimum relative differences are 0.6 (December 15) and 8.5

873    (January 3) (Table 1). Additionally, the differences are 0.5 (December 15) and 5.9 (January 3)

874    when applying the moderately-rimed S/Z relationship of Falconi et al. (results not shown).

875    Further research is needed to resolve the reason for the mismatch between the snowfall

876    rate/reflectivity pairs reported here and the S/Z relationships reported in Falconi et al.

877          Our conclusion that the upper-limit S/Z relationship from Hiley et al. (2011)

878    underestimates S would be modified if our WCR-derived reflectivities were negatively biased.

879    Assuming the reflectivities are negatively biased by 2.5 dBZ, the minimum relative differences

880    discussed previously change to 0.1 and 0.3 on 15 December and 3 January, respectively. A bias

881    in reflectivity of this magnitude cannot be ruled out but neither can a positive bias of the same

882    magnitude (Sect. 2.3). The latter increases the minimum relative differences to 1.6 and 2.2 on 15

883    December and 3 January, respectively. In each of these calculations we have summed the

884    attenuations (Table 4) with ± 2.5 dBZ and used Eq. 1 to calculate error-perturbed reflectivities.

885          The scatter of measurements in Fig. 12, the plausibility of a -2.5 to +2.5 dBZ bias in

886    WCR reflectivity measurements, and error in measurement of S (Sect. 2.4), indicate that refined

887    techniques will be needed in future investigations which apply the approach described here.

888    Taking into consideration the goal of evaluating snowfall rates from space, some advance in

889    satellite remote sensing also seems warranted. One issue is diagnosing where riming is occurring

890    within clouds. Both lidars and radiometers can sense supercooled liquid water from space (e.g.,

891  Battaglia and Panegrossi, 2020), and if combined with Doppler radars operating at multiple

892  wavelengths, can diagnose the presence of rimed precipitation particles. Despite limitations of

893  the multiple-wavelength Doppler method in scenarios with vertical air speed comparable to and

894  larger than particle fall speed (Vogl et al. 2022), the method has been validated in ground-based

895  field studies (Kneifel et al. 2015; Mason et al. 2018). Technical challenges also remain for

896  implementing the method from space (Battaglia et al. 2020).

**5 – Conclusions**

898  We have reported surface measurements of S and near-surface measurements of Z. The

899  latter came from overflights of a ground site, where a precipitation gauge was operated, and were

900  acquired using an airborne W-band radar. The values of Z were corrected for attenuation.

901  The reported $S_{HP}/Z'$ pairs plot at or above the S-versus-Z best-fit line of PV11 (Fig. 12)

902  and the minimum relative S difference (Table 1) is no larger than 0.3. The PV11 data came from

903  airborne measurements of W-band reflectivity, acquired within ± 100 m of flight level, and from

904  coincident measurements of snow particle imagery. PV11 used a density-size function, a fall

905  speed-size function, and measurements (PSD and particle images) to calculate S for snow

906  particles that were classified as both rimed crystals and graupel. This classification is also

907  consistent with the particle imagery we have presented (Fig. 11).

908  We have documented a substantial difference in comparisons between our snowfall rate

909  measurements and reflectivity-dependent snowfall rates calculated using an upper-limit S/Z

910  relationship (Hiley et al. 2011). This S/Z relationship produces an underestimate of the snowfall

911  rate (Fig. 12) when compared to our measurements. We also report substantial snowfall rate

912  underestimates in comparisons of our measurements to the S/Z relationship developed by

913     Matrosov (2007). The underestimates obtained using the Hiley et al. and Matrosov S/Z

914     relationships are perhaps expected given that the density factored into those S/Z calculations is

915     small compared to that for rimed snow particles. It is also expected that the larger density and

916     spherical shape applied in the SSKB S/Z relationship contributed to the better agreement seen in

917     the comparison of the SSKB relationship to our snowfall rate measurements. Our conclusion is

918     that some snowfall retrievals (e.g., Hiley et al. 2011) will underestimate S for weather targets

919     containing rimed snow particles. We also state that our conclusion is at odds with measurements

920     and analysis in Falconi et al. Those researchers reported S/Z relationships for rimed snow

921     particles which in instances with $Z < 8$ mm$^6$ m$^{-3}$ plot below the upper-limit of Hiley et al. (Fig.

922     12). A consequence is that the minimum relative S differences in our comparison to Falconi et al.

923     (assuming Falconi et al.'s heavily-rimed classification) is comparable to and larger than in our

924     comparison to Hiley et al.'s upper-limit S/Z relationship (Table 1).

925         New research is needed to refine the S/Z relationship for rimed snow particles. This could

926     be computational – e.g., investigation of the utility of parameterizing S in terms of both Z and

927     density – or could be observational. Unlike the investigation of PV11, where only an airborne

928     platform was employed, we have demonstrated that useful information can be obtained using

929     coordinated ground-based and airborne systems. Provided all key measurements are acquired (S,

930     PSD, particle imagery, and Z), another approach would be with only ground-based

931     instrumentation. This would avoid some of the complications encountered in this study,

932     including W-band attenuation and a reliance on particle imagery acquired aloft. A study with

933     both ground-based and airborne systems would also be useful for understanding an S/Z

934     mismatch apparent at $Z < 8$ mm$^6$ m$^{-3}$. Elements of the mismatch are the measurements reported

935     here, PV11's best-fit line, and the measurement-based S/Z relationships reported by Falconi et al.

936     (2018). These three research teams reported measurements relevant to the development of an S/Z

937     relationship for rimed snow particles.

938     **6 – Appendix**

939         This appendix explains how HP (hotplate) and WCR (Wyoming Cloud Radar) averages

940     were evaluated. The scheme starts with an HP averaging interval (duration 60 s) and derives a

941     WCR averaging interval and a WCR averaging domain. The latter encompasses a subset of the

942     altitude-time crossection sampled by the WCR. The top boundary of the domain was derived

943     using vertical-component Doppler velocities within the interval/domain. Because of this

944     dependence, the line defining the top boundary was derived iteratively.

945         With the overflight time symbolized $t_0$, the beginning and ending times of two 60-second

946     HP averaging intervals are

947         $$t_{HP,B} = t_O \tag{A1}$$

948         $$t_{HP,E} = t_O + 60 \tag{A2}$$

949         Since two adjacent HP averaging intervals are evaluated in this analysis, we express the

950     averaging times with the following recursive equations

951         $$t_{HP,B}(i) = t_O + i \cdot 60 \tag{A3}$$

952     and

953         $$t_{HP,E}(i) = t_O + (i+1) \cdot 60. \tag{A4}$$

954     In Eqs. A3-A4 the index is $i \in \{0, 1\}$. A special case with $i = 2$ is also analyzed (Sect. 3.5).

955     Analogous to the recursion in Eq. A4, the ending time of a WCR averaging interval is

956         $$t_{WCR,E}(i) = t_O - i \cdot 60 \cdot v_w / gs. \tag{A5}$$

957   Here $v_w$ is a wind advection speed (discussed below) and the second term on the rhs is a wind

958   advection distance divided by the WKA (Wyoming King Air) ground speed ($gs$). Analogous to

959   the Eq. A5, the beginning time of a WCR averaging interval is

960   $$t_{WCR,B}(i) = t_{WCR,E} - (i+1) \cdot 60 \cdot v_w / gs \qquad (A6)$$

961        The wind advection speed ($v_w$) in Eqs. A5-A6 was calculated using an altitude-

962   dependent west-to-east wind velocity ($u$) and an altitude-dependent south-to-north wind velocity

963   ($v$). These altitude-dependent component velocities were calculated using the horizontal wind

964   vectors in the penultimate and last columns of Table 3. Plots of the component velocities versus

965   altitude and the linear functions used to relate component velocities to altitude are presented in

966   Figs. A1a-b.

967        An altitude ($z' = 3400$ m) was assumed for evaluating the horizontal wind advection

968   vector. This is the altitude of the ridges west and northwest of the HP site (Figs. 3a-b).

969        The WKA track vector (Table 3) defines the vertical plane of the WCR measurements.

970   We assumed that wind advection of snow particles occurred parallel to this vector. With the

971   assumption stated in the previous paragraph, the horizontal wind advection speed ($v_w$) was

972   calculated as the projection of the horizontal wind vector onto the track vector.

973   $$v_w = \frac{u(z') \cdot gs_x + v(z') \cdot gs_y}{\left(gs_x^2 + gs_y^2\right)^{1/2}} \qquad (A7)$$

974   In Eq. A7 the west-to-east and south-to-north components of the track vector are symbolized $gs_x$

975   and $gs_y$. Vector representations of the track vector are in Table 3. On 14/15 December 2016 and

976   3 January 2017, the values of $v_w$ are 7.4 and 8.9 m s$^{-1}$, respectively.

977    In addition to the properties $gs$ and $v_w$ used to evaluate Eqs. A5-A6, a WCR averaging

978    interval/domain was evaluated using a snow particle downward speed (Eq. A8).

979         $$v_p = |<V_D>| + \sigma_{V_D} \qquad\qquad (A8)$$

980    Here, $<V_D>$ is the average of Doppler velocities within an averaging interval/domain,

981    $|<V_D>|$ is the absolute value of the average, and $\sigma_{V_D}$ is the standard deviation of the average.

982    On both the lhs and rhs of Eq. A8, all terms are greater than zero.

983         We interpret $v_p$ as the maximum likely snow particle speed toward the ground. There are

984    three reasons for this: 1) For the WCR averaging intervals/domains we analyzed, values of

985    $<V_D>$ were consistently less than zero (Table 6). This indicates that snow particles (on

986    average) were moving toward the ground. 2) Again, for the WCR averaging intervals/domains

987    we analyzed, $\sigma_{V_D}$ was comparable to $|<V_D>|$. This indicates that turbulent eddies transported

988    snow particles upward and downward at a speed comparable to their downward speed in still air.

989    3) The $V_D$ are reflectivity weighted (Haimov and Rodi 2013) and are thus indicative of the

990    motion of the largest particles within an averaging interval/domain.

991         We now focus on the top boundary of a WCR averaging interval/domain. Figures 6b and

992    6d have representations of the boundary. The slope defining this boundary was calculated as

993    $-v_p \cdot gs / v_w$. That is, particles below this boundary moved downward sufficiently fast and

994    horizontally sufficiently slow to advect reasonably close to the hotplate. Starting with diagnosed

995    values of $gs$ and $v_w$, the values of $v_p$ and slope, were derived iteratively. The precision of the

996    derived $v_p$ is $\pm 0.1$ m s$^{-1}$.

997

998
999
1000
1001
1002
1003
1004
1005

1006
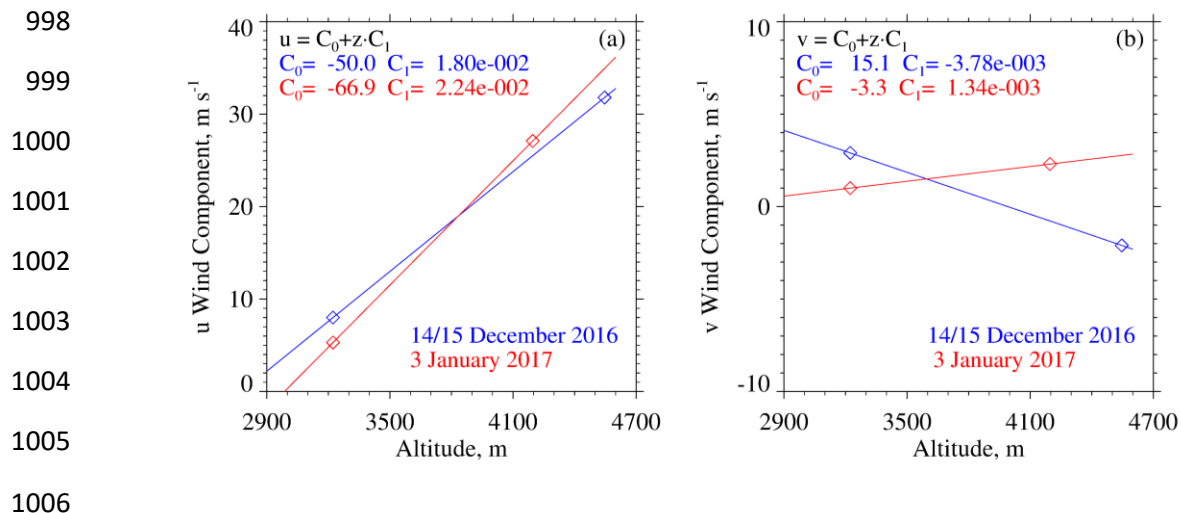
1007 Figure A1 – (a) West-to-east ($u$) wind velocity derived using measurements from the WKA and

1008 the AmeriFlux (AF) tower. Also shown is the linear function used to relate $u$ to altitude. (b)

1009 South-to-north ($v$) wind velocity derived using measurements from the WKA and AF. Also

1010 shown is the linear function used to relate $v$ to altitude. WKA and AF velocities are presented as

1011 vectors in the penultimate and last columns of Table 3.

1012

1013    Code/Date availability. The WKA and WCR measurements can be obtained from the SNOWIE

1014    data archive of NCAR/EOL, which is sponsored by the National Science Foundation. Hotplate

1015    gauge measurements are at https://doi.org/10.15786/20103146. The US-GLE AmeriFlux

1016    measurements are at https://ameriflux.lbl.gov/. The Brooklyn Lake SNOTEL gauge

1017    measurements are at https://www.wcc.nrcs.usda.gov/snow/. Merged Hotplate, SNOTEL, and

1018    AmeriFlux data sequences from 14/15 December 2016 and 3 January 2017 are in Snider (2023).

1019    Computer programs used to read, process, and plot the data are available on request from J.

1020    Snider.

1021    Author contributions. JS and MB wrote the grant proposal that funded this research. Field

1022    measurements were performed by SF, SM, SH, MB, and JS. SF wrote her MS dissertation, and

1023    this was adapted for this paper by JS. KS processed the snow particle imagery. AM maintained

1024    the measurement sites. All authors contributed to the editing of this paper.

1025

1026    Competing interests. The authors declare that they have no conflict of interest.

1027 **Acknowledgements –**

1028     We acknowledge technical assistance provided by David Plummer, Larry Oolman, Zane

1029 Little, Brent Glover, Edward Sigel, Thomas Drew, and Brett Wadsworth. We thank SNOWIE

1030 project PI Jeffery French, who provided the flight data, Gabor Vali who provided the S/Z data

1031 points in Fig. 12, and John Frank and John Korfmacher who acquired  the GLE-US AmeriFlux

1032 data set. This work was supported by the United States National Science Foundation (Award

1033 Number 1850809) and the John P. Ellbogen Foundation.

1034

**References**

AmeriFlux, https://ameriflux.lbl.gov/, 2021

Battaglia, A. and Panegrossi, G., What Can We Learn from the CloudSat Radiometric Mode Observations of Snowfall over the Ice-Free Ocean?, 12, 3285, https://doi.org/10.3390/rs12203285, 2020

Battaglia, A., Tanelli, S., Tridon, F., Kneifel, S., Leinonen, J., and Kollias, P, Triple-Frequency Radar Retrievals, In: Levizzani, V., Kidd, C., Kirschbaum, D.B., Kummerow, C.D., Nakamura, K., Turk, F.J. (eds) *Satellite Precipitation Measurement*, Advances in Global Change Research, vol 67. Springer, Cham. https://doi.org/10.1007/978-3-030-24568-9_13, 2020

Boudala, F.S., R. Rasmussen, G.A. Isaac, and B. Scott, Performance of Hot Plate for Measuring Solid Precipitation in Complex Terrain during the 2010 Vancouver Winter Olympics, J. Atmos. Oceanic Technol., 31, 437–446, https://doi.org/10.1175/JTECH-D-12-00247.1, 2014

Braham , R. R., Snow Particle Size Spectra in Lake Effect Snows. J. Appl. Meteor. Climatol., 29, 200–207, https://doi.org/10.1175/1520-0450(1990)029<0200:SPSSIL>2.0.CO;2, 1990

Brock, F. V., and Richardson, S. J., Meteorological Measurement Systems, Oxford University Press, New York, 304 pp., 2001

Brown, P. R. A., and P. N. Francis, Improved Measurements of the Ice Water Content in Cirrus Using a Total-Water Probe. J. Atmos. Oceanic Technol., 12, 410–414, https://doi.org/10.1175/1520-0426(1995)012<0410:IMOTIW>2.0.CO;2., 1995

Cocks, S.B., S.M. Martinaitis, B. Kaney, J. Zhang, and K. Howard, MRMS QPE Performance during the 2013/14 Cool Season, J. Hydrometeor., 17, 791–810, https://doi.org/10.1175/JHM-D-15-0095.1, 2016

Faber, S., French, J. R., and Jackson, R., Laboratory and in-flight evaluation of measurement uncertainties from a commercial Cloud Droplet Probe (CDP), Atmos. Meas. Tech., 11, 3645–3659, https://doi.org/10.5194/amt-11-3645-2018, 2018

Falconi, M. T., von Lerber, A., Ori, D., Marzano, F. S., and Moisseev, D.: Snowfall retrieval at X, Ka and W bands: consistency of backscattering and microphysical properties using BAECC ground-based measurements, Atmos. Meas. Tech., 11, 3059–3079, https://doi.org/10.5194/amt-11-3059-2018, 2018

1063    Field, P.R., Hogan, R.J., Brown, P.R.A., Illingworth, A.J., Choularton, T.W. and Cotton, R.J.,
1064        Parametrization of ice-particle size distributions for mid-latitude stratiform cloud. Q.J.R. Meteorol.
1065        Soc., 131: 1997-2017. https://doi.org/10.1256/qj.04.134, 2005

1066    Fuller, S.E., Improvement of the Snowfall / Reflectivity Relationship for W-band Radars, MS Thesis,
1067        Department of Atmospheric Science, University of Wyoming, 2020

1068    Geerts, B., Q. Miao, Y. Yang, R. Rasmussen, and D. Breed, An Airborne Profiling Radar Study of the
1069        Impact of Glaciogenic Cloud Seeding on Snowfall from Winter Orographic Clouds, J. Atmos. Sci.,
1070        67, 3286–3302, https://doi.org/10.1175/2010JAS3496.1, 2010

1071    Haimov, S., and Rodi, A., Fixed-Antenna Pointing-Angle Calibration of Airborne Doppler Cloud Radar,
1072        Journal of Atmospheric and Oceanic Technology, 30, 2320-2335, https://doi.org/10.1175/JTECH-
1073        D-12-00262.1, 2013

1074    Hiley, M. J., M. S. Kulie, and R. Bennartz, Uncertainty Analysis for CloudSat Snowfall Retrievals, J. Appl.
1075        Meteor. Climatol., 50, 399–418, 2011

1076    Kneifel, S., von Lerber, A., Tiira, J., Moisseev, D., Kollias, P., and Leinonen, J., Observed relations between
1077        snowfall microphysics and triple-frequency radar measurements. J. Geophys. Res. Atmos., 120,
1078        6034– 6055, doi: 10.1002/2015JD023156, 2015

1079    Kochendorfer, J., Nitu, R., Wolff, M., Mekis, E., Rasmussen, R., Baker, B., and Jachcik, A, Testing and
1080        development of transfer functions for weighing precipitation gauges in WMO-SPICE, Hydrology
1081        and Earth System Sciences, 2, 1437-1452, https://doi.org/10.5194/hess-22-1437-2018, 2018

1082    Korolev, A. V., E. F. Emery, J. W. Strapp, S. G. Cober, G. A. Isaac, M. Wasey, and D. Marcotte, Small ice
1083        particles in tropospheric clouds: Fact or artifact? Airborne Icing Instrumentation Evaluation
1084        Experiment, Bull. Amer. Meteor. Soc., 92, 967–973, https://doi.org/10.1175/2010BAMS3141.1,
1085        2011

1086    Kulie, M. S., and R. Bennartz, Utilizing Spaceborne Radars to Retrieve Dry Snowfall, J. Appl. Meteor.
1087        Climatol., 48, 2564–2580, https://doi.org/10.1175/2009JAMC2193.1, 2009

1088    Kulie, M. S., Milani, L., Wood, N. B., Tushaus, S. A., Bennartz, R., and L'Ecuyer, T. S., A Shallow
1089        Cumuliform Snowfall Census Using Spaceborne Radar, Journal of Hydrometeorology, 4, 1261-
1090        1279, https://doi.org/10.1175/JHM-D-15-0123.1, 2016

1091    Lawson, R. P., O'Connor, D., Zmarzly, P., Weaver, K., Baker, B., Mo, Q., and Jonsson, H., The 2D-S
1092        (Stereo) Probe: Design and Preliminary Tests of a New Airborne, High-Speed, High-Resolution

Particle Imaging Probe, J. Atmos. Ocean. Tech., 23, 1462–1477, https://doi.org/10.1175/JTECH1927.1, 2006

Liebe, H.J., Manabe, T., and Hufford, G.A., Millimeter–wave attenuation and delay rates due fog/cloud conditions, IEEE Trans. Antenn. Propag., 37, 1617–1623, 1989

Liu, C.-L., and A. J. Illingworth, Toward more accurate retrievals of ice water content from radar measurements of clouds, J. Appl. Meteor., 39, 1130–1146, 2000

Locatelli, J.D. and Hobbs, P.V., Fall speed and masses of solid precipitation particles, J. Geophys. Res., 79, 2185–2197, https://doi.org/10.1029/JC079i015p02185, 1974

Macklin, W.C., The density and structure of ice formed by accretion, Q.J.R.Meteorol.Soc., 88: 30-50. doi:10.1002/qj.49708837504, https://doi.org/10.1002/qj.49708837504, 1962

Marlow, S.A, J.M. Frank, M. Burkhart, B. Borkhuu, S.E. Fuller, and J.R. Snider, Snowfall Measurements at Wind-exposed and Sheltered Sites in the Rocky Mountains of Southeastern Wyoming, in revision for the Journal of Applied Meteorology and Climatology, http://www-das.uwyo.edu/~jsnider/manuscript_revision2.docx, 2023

Martinaitis, S.M., S.B. Cocks, Y. Qi, B.T. Kaney, J. Zhang, and K. Howard, Understanding winter precipitation impacts on automated gauge observations within a real-rime system, J. Hydrometeor., 16, 2345-2363, https://doi.org/10.1175/JHM-D-15-0020.1, 2015

Mason, S. L., Chiu, C. J., Hogan, R. J., Moisseev, D., and Kneifel, S., Retrievals of riming and snow density from vertically pointing Doppler radars, Journal of Geophysical Research: Atmospheres, 123, 13,807– 13,834, https://doi.org/10.1029/2018JD028603, 2018

Matrosov, S.Y., Modeling Backscatter Properties of Snowfall at Millimeter Wavelengths, J. Atmos. Sci., 64, 1727-1736, https://doi.org/10.1175/JAS3904.1, 2007

Nemarich, J., Wellman, R.J., and Lacombe, J., Backscatter and attenuation by falling snow and rain at 96, 140, and 225 GHz, IEEE Trans. Geosci. Remote, 26, 319–329, 1988

Panofsky, H.A. and Dutton, J.A., *Atmospheric Turbulence*, Wiley-Interscience, New York, 397 pp., 1984

Pokharel, B. and G. Vali, Evaluation of Collocated Measurements of Radar Reflectivity and Particle Sizes in Ice Clouds, J. Appl. Meteor. Climatol., 50, 2104–2119, https://doi.org/10.1175/JAMC-D-1005010.1, 2011

1121 Rasmussen, R.M., J. Hallett, R. Purcell, S.D. Landolt, and J. Cole, The Hotplate precipitation gauge, J.
1122     Atmos. Oceanic Technol., 28, 148-164, https://doi.org/10.1175/2010JTECHA1375.1, 2011

1123 R.M. Young Company, Model 05103 Wind Monitor, 2001

1124 Skofronick-Jackson, G., and Coauthors, The Global Precipitation Measurement (GPM) Mission for
1125     science and society, Bull. Amer. Meteor. Soc., 98, 1679–1695, https://doi.org/10.1175/BAMS-D-
1126     15-00306.1, 2017

1127 Smith, P.L., Equivalent radar reflectivity factors for snow and ice particles, J. Climatol. Appl. Meteor., 23,
1128     1258–1260, https://doi.org/10.1175/1520-0450(1984)023<1258:ERRFFS>2.0.CO;2, 1984

1129 Snider, J.R., Supplemental dataset for Marlow et al. (2023), https://doi.org/10.15786/20247870, 2023

1130 Surussavadee, C., and D. H. Staelin, Millimeter-Wave Precipitation Retrievals and Observed-versus-
1131     Simulated Radiance Distributions: Sensitivity to Assumptions. J. Atmos. Sci., 64, 3808–3826,
1132     https://doi.org/10.1175/2006JAS2045.1, 2007

1133 Tessendorf, S. A., and Coauthors, A transformational approach to winter orographic weather modification
1134     research: The SNOWIE Project, Bulletin of the American Meteorological Society, 100, 71–92,
1135     https://doi.org/10.1175/BAMS-D-17-0152.1, 2019

1136 Ulaby, F.T., Moore, R.K., and Fung, K., Microwave Remote Sensing: Active and Passive, Vol. 1,
1137     Microwave Remote Sensing Fundamentals and Radiometry, ARTECH HOUSE Inc., Norwood,
1138     MA, p. 456., 1981

1139 Vali, G. and Haimov, S., Observed extinction by clouds at 95 GHz, IEEE Trans. Geosci. Remote, 39, 190–
1140     193, 2001

1141 Vogl, T., Maahn, M., Kneifel, S., Schimmel, W., Moisseev, D., and Kalesse-Los, H.: Using artificial neural
1142     networks to predict riming from Doppler cloud radar observations, Atmos. Meas. Tech., 15, 365–
1143     381, https://doi.org/10.5194/amt-15-365-2022, 2022

1144 von Lerber, A., D. Moisseev, L. F. Bliven, W. Petersen, A. Harri, and V. Chandrasekar: Microphysical
1145     Properties of Snow and Their Link to Ze–S Relations during BAECC 2014. J. Appl. Meteor.
1146     Climatol., 56, 1561–1582, https://doi.org/10.1175/JAMC-D-16-0379.1, 2017

1147 Wang,Y., G.Liu, E.Seo, and Y.Fu, Liquid water in snowing clouds: Implications for satellite remote

1148 sensing of snowfall, Atmos. Res., 60-72, 10.1016/j.atmosres.2012.06.008, 2013

1149 Wang, P.K., and W. Ji, Collision Efficiencies of Ice Crystals at Low–Intermediate Reynolds Numbers
1150     Colliding with Supercooled Cloud Droplets: A Numerical Study, Journal of the Atmospheric
1151     Sciences, 57, 1001-1009, https://doi.org/10.1175/1520-0469(2000)057<1001:CEOICA>2.0.CO;2,
1152     2000

1153 Wilson, J., and E. Brandes, Radar measurement of rainfall—A summary, Bull. Amer. Meteor. Soc., 60,
1154     1048–1058, https://doi.org/10.1175/1520-0477(1979)060<1048:RMORS>2.0.CO;2, 1979

1155 Wolfe, J.P., and J.R. Snider, A relationship between reflectivity and snow rate for a high-altitude S-band
1156     radar, J. Appl. Meteor. Climatol., 51, 1111–1128, https://doi.org/10.1175/JAMC-D-11-0112.1,
1157     2012

1158 Zaremba, T.J., and Coauthors, Vertical motions in orographic cloud systems over the Payette River Basin.
1159     Part 1: Recovery of vertical motions and their uncertainty from airborne Doppler radial Velocity
1160     Measurements, in press at the Journal of Applied Meteorology and Climatology,
1161     https://doi.org/10.1175/JAMC-D-21-0228.1, 2022

1162 Zelasko, N., Wettlaufer, A., Borkhuu, B., Burkhart, M., Campbell, L. S., Steenburgh, W. J., and Snider,
1163     J.R., Hotplate precipitation gauge calibrations and field measurements, Atmos. Meas. Tech., 11,
1164     441-458, https://doi.org/10.5194/amt-11-441-2018, 2018

1165 Zikmunda, J. and Vali, G., Fall patterns and fall velocities of rimed ice crystals, J. Atmos. Sci., 29, 1334–
1166     1347, https://doi.org/10.1175/1520-0469(1972)029<1334:FPAFVO>2.0.CO;2, 1972

1167